

A New Method to Simulate Dark Matter–Baryon Interactions and Application to an Isolated Disk Galaxy

CONNOR HAINJE¹ AND GLENNYS R. FARRAR¹

¹*Center for Cosmology and Particle Physics, Department of Physics, New York University*

ABSTRACT

We report on a new method for incorporating interactions between dark matter (DM) and baryons in cosmological simulations, capable of handling the challenging regime in which the dark matter particle mass is comparable to or lighter than the baryon mass. The method hybridizes two distinct approaches: gas particles receive momentum and energy transfer according to a mean-field calculation while DM particles undergo Monte Carlo scatterings. These approaches are derived from the Boltzmann equation and shown to be statistically equivalent. We present an open-source implementation of this method in the simulation code GIZMO. As a first application, we investigate the effects of DM–baryon interactions on an isolated Milky Way-like disk galaxy for dark matter having twice the proton mass, which roughly maximizes the average energy transfer per collision. For cross sections of order 1 barn (10^{-24} cm²), these interactions cause strong changes to the mass distribution in the center of the galaxy in less than 1 Gyr, even when bar formation is suppressed by hand. For cross sections typical of hadronic interactions ($\lesssim 30$ mb), high-fidelity galaxy formation simulations will be needed to assess the effects on observable features of galaxies.

Keywords: Dark matter, Hydrodynamical simulations, N-body simulations, Galaxy dynamics, Particle astrophysics

1. INTRODUCTION

In the standard Lambda Cold Dark Matter (Λ CDM) paradigm, dark matter (DM) interacts only via gravity. This yields remarkably successful predictions on cosmological scales (e.g., [Planck Collaboration et al. 2020](#)), but tensions have been reported on smaller scales (e.g., [J. S. Bullock & M. Boylan-Kolchin 2017](#); [M. Kaplinghat et al. 2020](#)). Furthermore, some particle physics models imply potentially observable impacts of non-gravitational dark matter interactions: either DM self-interactions (SIDM; e.g., [D. N. Spergel & P. J. Steinhardt 2000](#); [S. Tulin & H.-B. Yu 2018](#); [S. Adhikari et al. 2025](#)) or DM interactions with the Standard Model (e.g., [C. Dvorkin et al. 2014](#); [G. R. Farrar 2022](#)). In this work, we focus on dark matter–baryon interactions, for which there has been a dearth of computational tools.

Dark matter–baryon (DM–b) interactions are a feature of many particle models of dark matter. The most common such model is the Weakly Interacting Massive Particle (WIMP), although it is not very interesting observationally due to its heavy mass, small cross section with baryons, and the severe constraints imposed by accelerator limits and direct detection experiments (e.g.,

[E. Aprile et al. 2023](#); [J. Aalbers et al. 2025](#)). We focus on dark matter with more observationally impactful interactions with baryons, such as the regime of light mass DM with moderate-to-strong interactions with baryons that is challenging to directly detect. In the GeV mass range, deep underground direct detection experiments like SuperCDMS are sensitive only to weak interactions (cross sections of 10^{-35} to 10^{-29} cm²) ([M. F. Albakry et al. 2023](#)), leaving the space $\gtrsim 10^{-28}$ cm² nearly unconstrained ([X. Xu & G. R. Farrar 2023](#)).²

A complementary approach to constraining DM–b interactions is through their astrophysical impacts. For example, [D. Wadekar & G. R. Farrar \(2021\)](#) placed limits by requiring that the heating or cooling due to DM–b interactions not exceed the radiative cooling rate of gas in gas-rich dwarf galaxies. DM–b interactions can also affect the structure of galaxies (e.g., [C. Dvorkin et al. 2014](#); [M. A. Buen-Abad et al. 2022](#)), primarily in two

² It has been proposed that the upscattering of DM by cosmic rays can enhance the sensitivity of direct detection experiments ([J. Alvey et al. 2023](#)), which could significantly constrain the parameter space in this range after non-resonant energy losses in propagation through the Earth are accounted for.

ways: by introducing viscosity before recombination and thereby suppressing the power spectrum on small scales, and by changing the formation and evolution of galaxies. The pre-recombination imprints have been used to place limits on interaction parameters by comparing against measurements of the CMB (V. Gluscevic & K. K. Boddy 2018; K. K. Boddy & V. Gluscevic 2018; K. K. Boddy et al. 2018; Y. Ali-Haïmoud et al. 2024), the Lyman- α forest (C. Dvorkin et al. 2014; W. L. Xu et al. 2018), large-scale structure (A. He et al. 2023, 2025), and the abundance of Milky Way satellites (E. O. Nadler et al. 2021; K. Maamari et al. 2021; M. A. Buen-Abad et al. 2022).

An important caveat to these galactic structure analyses is that the effects of DM–b interactions during the non-linear regime of structure formation are generally neglected. This is largely because a detailed treatment requires resolving the interplay between these interactions and baryonic physics, which is very challenging. For example, DM–b interactions can provide a new, diffuse source of heating, which may moderate star formation and affect feedback from active galactic nuclei and supernovae. DM–b interactions could also change the shape and kinematics of dark matter halos. These effects cannot be treated in isolation. Further, Λ CDM predictions in this regime commonly rely on “gastrophysics” prescriptions like subgrid models, many of which are tuned to reproduce the observed distribution of galaxies, and so potentially can be re-tuned to reproduce the observations in the presence of DM–b interactions. Careful consideration of this re-tuning will be important when using observations to test for and limit DM–b interactions.

The purpose of our work is to develop tools to enable an accurate treatment of the effects of dark matter–baryon interactions during galaxy formation and evolution. We have developed a new method for incorporating DM–b interactions into hydrodynamic cosmological simulations, which we have implemented as a module in the code GIZMO (P. F. Hopkins 2015). We focus on elastic scatterings between non-relativistic dark matter and baryon particles with a phenomenological, isotropic power-law cross section $\sigma(v) = \sigma_0 (v/c)^n$, where $v \ll c$ is the relative velocity, though we note that our methods can be applied to general cross section dependencies on v and scattering angle. The method hybridizes two statistically equivalent but qualitatively different approaches: the dark matter is treated in a Monte Carlo fashion, where simulation particles probabilistically undergo scatterings, and the baryons are treated with a mean-field approach, where the statistical expectations for the transfer rates of bulk velocity and thermal en-

ergy are applied. These are both derived directly from the Boltzmann equation and proven to conserve energy and momentum in expectation.

During the preparation of this article, we learned of a parallel effort to implement DM–b interactions in N -body simulations (M. S. Fischer et al. 2025) (F25 below). The advantages and disadvantages of that approach relative to ours are discussed in Section 2.5. The most significant difference is that the F25 approach requires the dark matter and baryon macroparticle masses to satisfy $M_\chi/M_b < 3/28 (m_\chi/m_b) \approx 0.1 m_\chi/\text{GeV}$, so employing the F25 method in the $m_\chi \lesssim \text{few GeV}$ regime requires a much larger number of dark matter macroparticles than for non-interacting DM.³

Our method thus provides for the first time a practical tool for investigating dark matter–baryon interactions for a dark matter mass close to that of hydrogen and helium, where energy and momentum transfer in individual collisions is maximally efficient. A concrete example of such a model is Sexaquark Dark Matter, in which the dark matter particle is a six-quark state ($uuddss$) whose binding is sufficiently deep that it is effectively stable; see G. R. Farrar (2022) and references therein for a review of the constraints from particle physics, astrophysics, and cosmology, and M. Moore & S. Profumo (2025) for additional discussion.

As an initial application of our code, we simulate the isolated Milky Way-like disk galaxy of the AGORA project (J.-h. Kim et al. 2016) with a dark matter particle having twice the proton mass ($2 m_p$) and velocity-independent cross section. We find that sufficiently strong dark matter–baryon interactions induce significant changes to the morphology of the center of the galaxy, driving gas and dark matter inflows toward the center. For potentially realistic DM–b cross sections below tens of millibarns, assessing the impact of dark matter–baryon interactions will require more detailed treatment of star formation, feedback, and the hierarchical formation of galaxies than we undertake in the present work.

The article is structured as follows. Section 2 gives the relevant scattering theory and the algorithms used to implement our approach in code. Section 3 briefly discusses the tests we perform to validate our implementation. Section 4 presents the key results of our simulation of the AGORA disk galaxy. Section 5 concludes. Ap-

³ For reference, state-of-the-art cosmological simulations adopt $M_\chi/M_b \approx 5$ (e.g., P. F. Hopkins et al. 2018; D. Nelson et al. 2019, 2024), and some isolated galaxy sims choose ratios as high as $M_\chi/M_b \approx 100$ (J.-h. Kim et al. 2016).

pendices provide derivations and details about our test suite.

2. METHOD

In this section, we derive our method and discuss our implementation. We begin by establishing the Boltzmann equation of our simulations using three core assumptions that underpin N -body simulations. We use this Boltzmann equation to derive both a probabilistic scattering treatment for dark matter, and the mean acceleration and heating rates for baryons. Then, we describe our implementation of this method in the simulation code GIZMO, and finally we provide a detailed comparison of our method with that of [M. S. Fischer et al. \(2025\)](#).

2.1. Boltzmann equation

We consider elastic $2 \leftrightarrow 2$ collisions between non-relativistic dark matter particles (of mass m_χ) and baryons (of mass m_B) with differential cross section $d\sigma/d\Omega(v_{\text{rel}}, \theta)$. In any individual scatter with initial velocities $\mathbf{v}_\chi, \mathbf{v}_B$, the outgoing velocities are given by

$$\mathbf{v}'_\chi \equiv \mathbf{S}_\chi = \mathbf{v}_\chi + \frac{m_B}{m_\chi + m_B} v_{\chi B} [\hat{\mathbf{v}}'_{\chi B} - \hat{\mathbf{v}}_{\chi B}], \quad (1)$$

$$\mathbf{v}'_B \equiv \mathbf{S}_B = \mathbf{v}_B - \frac{m_\chi}{m_\chi + m_B} v_{\chi B} [\hat{\mathbf{v}}'_{\chi B} - \hat{\mathbf{v}}_{\chi B}], \quad (2)$$

where $\mathbf{v}_{\chi B} \equiv \mathbf{v}_\chi - \mathbf{v}_B$, $v_{\chi B} = |\mathbf{v}_{\chi B}|$, $\hat{\mathbf{v}}_{\chi B} = \mathbf{v}_{\chi B}/|\mathbf{v}_{\chi B}|$, and $\hat{\mathbf{v}}'_{\chi B}$ is a new direction. The scattering angle θ describes the angle between the two unit vectors $\hat{\mathbf{v}}_{\chi B}$ and $\hat{\mathbf{v}}'_{\chi B}$: $\cos \theta = \hat{\mathbf{v}}_{\chi B} \cdot \hat{\mathbf{v}}'_{\chi B}$. We introduce \mathbf{S}_χ and \mathbf{S}_B , which may be thought of as functions of $\mathbf{v}_\chi, \mathbf{v}_B, \Omega$, as a short notation representing this transformation.

In the continuum limit, dark matter and baryons are each described by a distribution function⁴ (DF) $f(\mathbf{x}, \mathbf{v})$ whose evolution is governed by the Boltzmann equation:

$$\begin{aligned} \frac{df_\chi}{dt}(\mathbf{v}_\chi) &= \int d^3v_B d\Omega \frac{d\sigma}{d\Omega} v_{\chi B} \\ &\times [f_\chi(\mathbf{S}_\chi) f_B(\mathbf{S}_B) - f_\chi(\mathbf{v}_\chi) f_B(\mathbf{v}_B)], \end{aligned} \quad (3)$$

where the dependence on \mathbf{x} is implicit. The right-hand side of this equation is known as the collision integral.

Our goal is to implement the effects of these collisions in a Lagrangian-picture hydrodynamic cosmological simulation. Such simulations are built on three approximations, which we will use to derive our method.

The first approximation made by all N -body simulations is that the dark matter is a “softened N -body

component”; namely, a number of Monte Carlo samples are drawn from some true initial DF f_χ and spatially convolved with a smoothing kernel $W(r)$,⁵ producing the following approximate DF

$$\hat{f}_\chi(\mathbf{x}, \mathbf{v}) = \sum_{i=1}^{N_\chi} \frac{M_i}{m_\chi} W(|\mathbf{x} - \mathbf{x}_i|, h_i) \delta(\mathbf{v} - \mathbf{v}_i). \quad (4)$$

This can be understood as representing the dark matter by N_χ “macroparticles”, each having a mass M_i , position \mathbf{x}_i , smoothing length h_i , and velocity \mathbf{v}_i .

The second approximation is that the gas is represented by a thermalized softened N -body component. By this, we mean that the gas is decomposed into macroparticles like dark matter, but each macroparticle has a bulk velocity and internal energy describing the velocity distribution, which is locally Maxwell-Boltzmann at all times. Therefore, the gas is represented by the approximate DF⁶

$$\hat{f}_B(\mathbf{x}, \mathbf{v}) = \sum_{j=1}^{N_B} \frac{M_j}{\mu_j} W(|\mathbf{x} - \mathbf{x}_j|, h_j) \mathcal{G}(\mathbf{v} - \mathbf{V}_j, T_j/\mu_j), \quad (5)$$

where \mathcal{G} is the probability density function of a three-dimensional isotropic Gaussian—i.e., the Maxwell-Boltzmann distribution. In simulation, the gas is represented by N_B macroparticles, each having a mass M_j , position \mathbf{x}_j , smoothing length h_j , bulk velocity \mathbf{V}_j , and temperature T_j . Gas macroparticles can also consist of different species of particles; we approximate the dark matter as having equal cross section with all species, so all that matters is the mean molecular weight, μ_j .

The macroparticle DFs for dark matter and gas have a similar form. For brevity, we introduce the following notation:

$$\hat{f}(\mathbf{x}, \mathbf{v}) = \sum_i n_i(\mathbf{x}) \nu_i(\mathbf{v}), \quad (6)$$

where n_i is a number density and ν_i is a probability density function for the velocities, equal to either a Dirac

⁵ We assume throughout that any valid smoothing kernel $W(r, h)$ integrates to 1 and is zero (or else negligible) for $r > h$.

⁶ We note that this form of the baryon DF is valid for any hydrodynamic solver. By computing the moments of the baryon-baryon Boltzmann equation for this DF, one can derive the fluid equations for standard smoothed particle hydrodynamics (e.g., [J. J. Monaghan 1992](#)). More modern solvers, such as the moving Voronoi mesh of AREPO ([V. Springel 2010](#)) or the meshless methods of GIZMO ([P. F. Hopkins 2015](#)), generally assume more sophisticated geometries for the discretization of the gas. However, in these simulations the resulting particle distribution is then taken to have the form of Equation 5 for other applications, such as solving gravity, and so we take this form for solving interactions with dark matter.

⁴ We use the convention $\int d^3x d^3v f(\mathbf{x}, \mathbf{v}) = \mathcal{N}$, the total number of particles. The number density is then given by $n(\mathbf{x}) = \int d^3v f(\mathbf{x}, \mathbf{v})$.

delta (for dark matter) or a Maxwell-Boltzmann distribution (for gas).

The third approximation underpinning these simulations is made by assuming that the time-evolution of the true DFs f_χ, f_B is well-approximated even when enforcing that the form of the macroparticle DFs \hat{f}_χ, \hat{f}_B is preserved. In other words, after a timestep, the forms of Equations 4 and 5 can be imposed on the dark matter and gas, albeit with updated values of the parameters. We make this point explicit because the full evolution of the DF according to the Boltzmann equation would distort the functional form of the discretization—for example, the softened macroparticles would experience tidal forces and become stretched and sheared—but this is regularly ignored. For our purposes, this assumption means that evolution according to the collision integral only updates the local velocity distributions of the individual particles. Thus, the Boltzmann equation is

$$\begin{aligned} \sum_i n_i(\mathbf{x}) \frac{d\nu_i}{dt} \Big|_{\mathbf{v}_\chi} & \quad (7) \\ &= \sum_{i,j} n_i(\mathbf{x}) n_j(\mathbf{x}) \int d^3v_B d\Omega \frac{d\sigma}{d\Omega} v_{\chi B} \\ & \quad \times [\nu_i(\mathbf{S}_\chi) \nu_j(\mathbf{S}_B) - \nu_i(\mathbf{v}_\chi) \nu_j(\mathbf{v}_B)], \end{aligned}$$

and similarly for the baryons.

The form of this equation suggests a matching procedure: term i on the left-hand side can be set equal to term i on the right-hand side. By doing this matching, we are making an additional assumption: that the phase space densities of macroparticles of the same type do not mix, so each macroparticle evolves as if it is the

only particle of its type at its location. This assumption is reasonable as long as no particles have identical positions \mathbf{x} , which is already required for the validity of the N -body approach. Hence, individual macroparticles evolve according to independent collision integrals:

$$\begin{aligned} \frac{df_\chi^i}{dt}(\mathbf{v}_\chi) &= \int d^3v_B d\Omega \frac{d\sigma}{d\Omega} v_{\chi B} \\ & \quad \times [f_\chi^i(\mathbf{S}_\chi) \hat{f}_B(\mathbf{S}_B) - f_\chi^i(\mathbf{v}_\chi) \hat{f}_B(\mathbf{v}_B)], \end{aligned} \quad (8)$$

with \mathbf{x} -dependence implicit and defining $f_\chi^i(\mathbf{x}, \mathbf{v}) \equiv n_i(\mathbf{x}) \nu_i(\mathbf{v})$. This equation applies analogously to the baryons.

2.2. Dark matter evolution

In order to determine how to update the velocities of the dark matter particles, consider a finite timestep Δt . To first order in the timestep, the updated DF is

$$f_\chi^i \Big|_{t+\Delta t} = f_\chi^i \Big|_t + \frac{df_\chi^i}{dt} \Big|_t \Delta t, \quad (9)$$

where we require $f_\chi^i|_{t+\Delta t}$ to have the form $n_i(\mathbf{x}) \nu'_i(\mathbf{v})$, for ν'_i the new velocity distribution of the particle.

The derivation proceeds from here in detail in Appendix A. Briefly, the steps we take are as follows. We substitute into Equation 9 the baryon macroparticle DF \hat{f}_B . This gives a sum over gas particles j , each with a different integral over $d^3v_B d\Omega$. We simulate this integral by drawing a single Monte Carlo sample independently for every j (denoting the sampled baryon velocity \mathbf{v}_{ij}^B and scattering angles Ω_{ij}). Then, in order to isolate the velocity distribution on both sides, we integrate both sides over all space. The result is

$$\nu'_i(\mathbf{v}) = \left(1 - \sum_j P_{ij}\right) \delta(\mathbf{v} - \mathbf{v}_i) + \sum_j P_{ij} \delta(\mathbf{v} - \mathbf{S}_\chi(\mathbf{v}_i, \mathbf{v}_{ij}^B, \Omega_{ij})), \quad \text{where} \quad (10)$$

$$P_{ij} \equiv \frac{M_j}{\mu_j} g_{ij} \sigma(v_{\text{rel}}) v_{\text{rel}} \Delta t, \quad g_{ij} \equiv \int d^3x W(|\mathbf{x} - \mathbf{x}_i|, h_i) W(|\mathbf{x} - \mathbf{x}_j|, h_j), \quad \sigma(v) \equiv \int d\Omega \frac{d\sigma}{d\Omega} \Big|_v, \quad (11)$$

and $v_{\text{rel}} \equiv |\mathbf{v}_i - \mathbf{v}_{ij}^B|$. Note the appearance of the total cross section $\sigma(v)$. We have introduced two intermediate variables to clarify the meaning of this result. One is g_{ij} , introduced by M. Rocha et al. (2013) for self-interacting dark matter simulations and dubbed the “geometric factor” or the “overlap integral”. It has dimensions of inverse volume and gives the effective number density of particle j acting on particle i . The other is P_{ij} , which is dimensionless and, as long as $P_{ij} \ll 1$, can be understood as a probability. Indeed, $(M_j/\mu_j) g_{ij}$ is the

effective number density of microscopic baryons active in this interaction, so P_{ij} has the form $n \sigma v \Delta t$, exactly as one would expect.

The new velocity distribution ν'_i is a discrete probability distribution: it gives the post-scattering velocity $\mathbf{S}_\chi(\mathbf{v}_i, \mathbf{v}_{ij}^B, \Omega_{ij})$ with probability P_{ij} , or the original velocity \mathbf{v}_i with probability $1 - \sum_j P_{ij}$. To pick a new velocity for macroparticle i , we can draw a sample from this discrete distribution. Notice that the time-evolution of the dark matter macroparticles is given by probabilis-

tically scattering them off samples from the baryon velocity distribution in a manner that agrees exactly with the microscopic theory.

2.3. Baryon evolution

We next consider the updates to apply to the baryons. The updated baryon velocity distribution is required to remain Maxwell-Boltzmann. This suggests an alternative approach in which we directly compute the rates-of-change of the parameters of the Maxwell-Boltzmann dis-

tribution: the bulk velocity and the temperature. These are

$$n_j(\mathbf{x}) \frac{d\mathbf{V}_j}{dt} = \int d^3v_B \left. \frac{df_B^j}{dt} \right|_{\mathbf{x}, v_B} \mathbf{v}_B, \quad (12)$$

$$n_j(\mathbf{x}) \frac{3}{\mu_j} \frac{dT_j}{dt} = \int d^3v_B \left. \frac{df_B^j}{dt} \right|_{\mathbf{x}, v_B} (\mathbf{v}_B - \mathbf{V}_j)^2. \quad (13)$$

These can be evaluated using techniques very similar to those described by Y. Ali-Haïmoud (2019), augmented by an integral over space (like in the dark matter case). Details are provided in Appendix B. The result is

$$\frac{d\mathbf{V}_j}{dt} \approx \sum_i \frac{M_i}{m_\chi + \mu_j} g_{ij} \mathcal{A}(\mathbf{v}_i - \mathbf{V}_j; T_j/\mu_j) (\mathbf{v}_i - \mathbf{V}_j), \quad (14)$$

$$\frac{3}{2\mu_j} \frac{dT_j}{dt} \approx \sum_i \frac{M_i}{m_\chi + \mu_j} g_{ij} \left[(\mathbf{v}_i - \mathbf{V}_j)^2 \mathcal{A}(\mathbf{v}_i - \mathbf{V}_j; T_j/\mu_j) - \frac{\mu_j}{m_\chi + \mu_j} \mathcal{B}(\mathbf{v}_i - \mathbf{V}_j; T_j/\mu_j) \right], \quad (15)$$

where g_{ij} is the overlap integral as before and \mathcal{A} and \mathcal{B} are defined:

$$\mathcal{A}(\mathbf{w}; \zeta^2) \equiv \int d^3u \mathcal{G}(\mathbf{w} - \mathbf{u}, \zeta^2) u \frac{\mathbf{u} \cdot \mathbf{w}}{w^2} \bar{\sigma}(u), \quad (16)$$

$$\mathcal{B}(\mathbf{w}; \zeta^2) \equiv \int d^3u \mathcal{G}(\mathbf{w} - \mathbf{u}, \zeta^2) u^3 \bar{\sigma}(u), \quad (17)$$

$$\bar{\sigma}(v) = \int d\Omega \left. \frac{d\sigma}{d\Omega} \right|_v (1 - \cos\theta). \quad (18)$$

Notice the appearance of the momentum transfer cross section, $\bar{\sigma}$. If the momentum transfer cross section has a power-law dependence on v , then these integrals \mathcal{A} and \mathcal{B} have simple forms in terms of special functions, given in Appendix B. In simulation, these rates-of-change can be treated directly as new sources of acceleration and heating, added onto the total acceleration and heating rates, which are already accumulated for each particle and integrated by the preferred scheme of the simulation.

These rates-of-change are statistically equal and opposite to the Monte Carlo sampling procedure we have outlined for the dark matter. Momentum and energy are conserved in expectation value, which we prove in Appendix C.

We note that the dark matter and baryon calculations end up using *different* integrals over the differential cross section: the dark matter scattering probability depends on the total cross section σ , while the gas exchange rates depend on the momentum transfer cross section $\bar{\sigma}$. In the self-interacting dark matter literature, it is often assumed that one can approximate a non-isotropic cross

section in the scattering probability by using isotropic scatterings with the momentum transfer cross section (S. Tulin & H.-B. Yu 2018). For dark matter–baryon interactions, such an assumption must be carefully considered, as it could break the equivalence between the two calculations.

2.4. GIZMO implementation

We implement this method in GIZMO (P. F. Hopkins 2015), which is based in part on the algorithms of GADGET-2 (V. Springel 2005). We choose to specialize to an isotropic power-law cross section $\sigma(v) = \bar{\sigma}(v) = \sigma_0 (v/c)^n$. We note that other cross sections, including non-isotropic ones, can be implemented in this framework with relative ease, so long as the integrals defining \mathcal{A} and \mathcal{B} can be computed efficiently.

The core of the implementation is a nearest-neighbors calculation, where dark matter particles seek gas particles and vice versa, during the “kick” step of the GIZMO leapfrog integrator. Each particle searches in a radius equal to twice its softening length. With this search radius, each pair of particles that overlaps is guaranteed to be found by the neighbor with larger softening length, but may or may not be found by the smaller neighbor. Accordingly, we must search in both directions (dark matter \rightarrow gas and vice versa); to ensure that each pair is processed only once, we skip a pair whenever the *searching* particle has the smaller softening length.

To process pair (i, j) (taking i to be dark matter, j gas), we first compute the overlap integral g_{ij} . We then compute the contribution of particle i to the accelera-

tion $d\mathbf{V}_j/dt$ and heating rate dT_j/dt of particle j , which are accumulated over all pairs that include j . Next, we draw a random sample from the gas velocity distribution $\mathcal{G}(\mathbf{v} - \mathbf{V}_j, T_j/\mu_j)$ and use it to compute the scattering probability P_{ij} . If the scattering probability P_{ij} is too large, we reduce the timestep size for the dark matter particle for the next timestep. The criterion we use is

$$P_{ij} < \min\left(0.1, 10^{-4} \left[\frac{m_\chi + \mu_j}{\mu_j}\right]^2\right), \quad (19)$$

which requires smaller timesteps if $m_\chi \lesssim \mu_j$ (because in that case scatters are expected to impart a large change on the dark matter velocity).⁷ We draw a random number r uniformly between 0 and 1 to decide whether to scatter the dark matter particle. If we choose to scatter (if $r < P_{ij}$), we choose a new direction $\hat{\mathbf{v}}'_{\chi B}$ isotropically, then compute \mathbf{v}'_χ from Equation 1 and apply it to particle i .

An important detail in the implementation is the computation of the confluent hypergeometric function ${}_1F_1(a, b; x)$. As given in Appendix B, the integrals \mathcal{A} and \mathcal{B} reduce to simple forms involving ${}_1F_1$ for our chosen cross section. We exclusively use this function in the regime of small a , small b , and negative x . However, the GSL implementation of this function is subject to overflow at modestly large values of $-x$. We can improve the performance for this specific regime by making use of Kummer’s transformation and the asymptotic expansion for large values of x (DLMF 2025, Equations 13.2.39 and 13.7.2). Together, these give the following expansion:

$${}_1F_1(a, b; -x) = \frac{\Gamma(b) x^{-a}}{\Gamma(b-a)} \sum_{k=0}^{\infty} \frac{(a)_k (1+a-b)_k}{k! x^k}, \quad (20)$$

where $(\cdot)_k$ is the Pochhammer symbol. In our implementation, we switch to this expansion whenever $|x| \geq 50$ (using the GSL implementation otherwise), truncating the sum at five terms. This gives fractional errors of less than 10^{-14} for all x of interest when compared against the Boost Math library implementation.⁸

Another important implementation detail is the computation of the overlap integral g_{ij} . It is too expensive to compute as needed at runtime, but it can be tabulated ahead of time for the chosen softening kernel, as it

depends only on the distance between the two particles and the ratio of their softening lengths. This is done via a technique similar to that described by M. S. Fischer et al. (2025); details are given in Appendix D.

Lastly, we note that our implementation properly accounts for the conversion from comoving to physical coordinates and the Hubble flow in GIZMO, although this is not directly tested in the simulations in this paper.

Our implementation is open-source under the GNU General Public License and is publicly available on GitHub.⁹

2.5. Comparison to existing methods

The method we use for dark matter is very similar to methods for simulating self-interacting dark matter (e.g., M. Rocha et al. 2013). Our treatment of baryons borrows much technology from analyses of dark matter–baryon interactions in linear cosmology (e.g., C. Dvorkin et al. 2014; Y. Ali-Haïmoud 2019). At the time of publication of this article, however, the only existing method specifically designed for simulating dark matter–baryon interactions is that of M. S. Fischer et al. (2025) (F25). We give in this section a detailed comparison of our method to the F25 scheme for “rare, large-angle scatters”; F25 also gives a scheme for “frequent, small-angle scatters” specialized to a certain class of cross section, which largely avoids the pitfalls we describe but is not analogous to our method.

At a high level, F25 and this work treat dark matter the same way. In both methods, dark matter particles scatter with neighboring baryon particles with probability $(M_B/m_B) g_{ij} \sigma v \Delta t$. Further, both sample the scattering baryon velocity \mathbf{v}_B from the Maxwell-Boltzmann distribution described by the bulk velocity and internal energy of the neighbor gas particle.

The key difference is our handling of baryons. We use the fact that the baryon velocity distribution remains Maxwell-Boltzmann at all times to calculate moments of the Boltzmann equation. This gives us momentum and heat transfer rates that can be directly applied to the gas macroparticles. F25 instead develops a scheme to apply the probabilistic scatters to the baryons. The issues they must solve, and which we sidestep, are how to conduct a scattering between macroparticles that represent (1) different numbers of physical particles (i.e., when $M_\chi/m_\chi \neq M_B/m_B$), and (2) different kinds of velocity distributions (i.e., Dirac delta for dark matter and Maxwell-Boltzmann for baryons). F25 handles these issues by constructing a “virtual” baryon particle for scattering. The virtual particle has mass M_{virt} set so that

⁷ Note that the sum $\sum_j P_{ij}$ should also remain small. For $m_\chi = 2m_p$, Equation 19 imposes a maximum of $P_{ij} \lesssim 10^{-3}$, with most probabilities significantly less than this threshold, so this is safely satisfied in our simulations.

⁸ See the Boost library’s excellent discussion of the methods they employ to calculate this function accurately: https://www.boost.org/doc/libs/latest/libs/math/doc/html/math_toolkit/hypergeometric/hypergeometric_1f1.html.

⁹ <https://github.com/cmhainje/gizmo-public>

$M_{\text{virt}}/m_B = M_\chi/m_\chi$, which makes it straightforward to apply a scattering. After scattering, the changes in momentum and energy of the virtual particle are distributed back to the simulation baryon particle, which makes use of the Maxwell-Boltzmann distribution nature of baryon macroparticles.

The virtual baryon approach has a few key advantages. One is that it is marginally more efficient: baryons are only updated when a partner dark matter particle is updated, and these updates do not require the calculation of any special functions. Another is that energy and momentum are conserved on a per-scattering basis. We contrast these against our code, where baryons receive small, smooth updates every timestep, these updates require calculating special functions, and the split approach means we can only conserve energy and momentum on average.

The primary difficulty with the virtual baryon approach is ensuring that the internal energy of the simulation particle remains positive after the scattering. This is enforced by rejecting scatterings whenever they result in a negative internal energy. The rate of these rejections primarily depends on how the mass ratio of the macroparticles, M_χ/M_B , compares to that of the true particles, m_χ/m_B . If a large fraction of scatters are rejected, the energy transfer between species will be biased.

We have performed a numerical experiment using the F25 algorithm to determine what macroparticle mass ratios are valid for a range of true particle mass ratios. A detailed discussion of our numerical experiment is given in Appendix E. The rate at which scatters are rejected and the resulting bias of the overall energy transfer are shown in Figure 1. The vertical bar denotes the upper boundary of the “safe zone” given in Equation 12 of F25; one sees that their safe zone is robust and even conservative by a factor of 2, depending on the accuracy required. In general, the accuracy of the F25 virtual baryon approach rapidly and severely degrades whenever $M_\chi/M_B \gtrsim \frac{1}{3} m_\chi/m_B$.

For small dark matter particle masses, $m_\chi \lesssim m_B$, restricting to the safe zone means that the dark matter macroparticles need much lower mass (i.e., higher resolution) than baryons. Such a requirement is computationally infeasible in many cosmological and galaxy simulations, where the dark matter is the dominant component of the simulation by mass and high resolution for the baryons is needed. Because our method makes different trade-offs, it remains accurate even in the $M_\chi/M_B \gtrsim m_\chi/m_B$ regime.

In summary, the F25 approach has computational advantages, including exact conservation of momentum

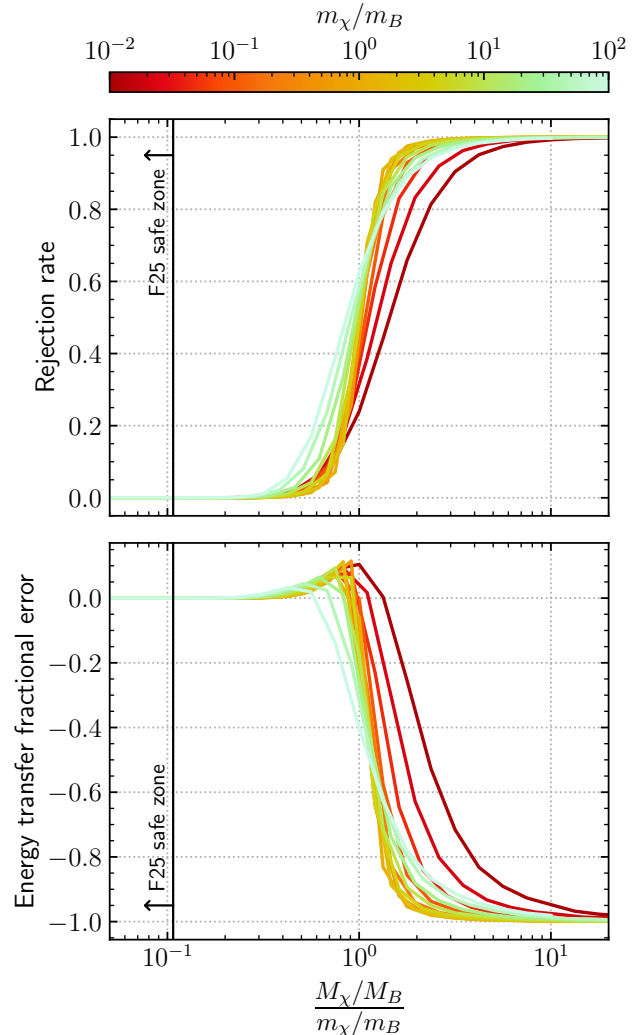


Figure 1. The rejection rate (top) and fractional error of the energy transfer (bottom) for the *M. S. Fischer et al. (2025)* (F25) method as a function of the macroparticle mass ratio M_χ/M_B divided by the physical particle mass ratio m_χ/m_B . The region that is expected to be “safe” according to Equation 12 of F25 is marked with a vertical line and a leftward arrow. In agreement with this expectation, we find that the algorithm is valid whenever $M_\chi/M_B \ll m_\chi/m_B$, as the rejection rate is negligible and the energy transfer matches the expectation. For $M_\chi/M_B \gtrsim m_\chi/m_B$, the transition to rejecting nearly all scatters happens rather abruptly, leading to a severe underestimate of the energy transfer rate.

and energy, which in some regimes make it more efficient than the method we have developed. However, F25 is only accurate when the $M_\chi/M_B \lesssim \frac{1}{3} m_\chi/m_B$. For small dark matter masses $m_\chi \lesssim m_B$, this restriction would make many cosmological simulations infeasible. However, our method remains accurate without this restriction, enabling much lower computational cost. Further, as will be described below, we find nearly identical per-

formance to the F25 method in a test problem where the F25 method is accurate.

3. TESTS

We have verified our implementation by constructing a test problem that isolates the dark matter–baryon interactions. Explicit details and results are given in Appendix F; we present a brief summary here. The test problem consists of a box with periodic boundary conditions filled uniformly with dark matter and gas of specified densities. The gas particles start at rest and are given some initial internal energy. The dark matter particles are given velocities sampled from a Maxwell-Boltzmann distribution with some bulk velocity and effective temperature. All physics modules in GIZMO are disabled except for dark matter–baryon interactions. We test a wide variety of initial conditions and mass resolutions for our fiducial dark matter model, which has mass $m_\chi = 2m_p$ and velocity-independent cross section $\sigma = 10 \text{ mb}$ (10^{-26} cm^2). We also test alternative dark matter models for a limited set of initial conditions, including different dark matter masses, $m_\chi \in \{10 \text{ GeV}, 100 \text{ MeV}, 10 \text{ MeV}\}$, and velocity-dependent cross sections, $n \in \{-2, -4\}$.

The test problem is designed to facilitate comparison to a direct numerical integration of a system of differential equations derivable under the assumption that the dark matter is Maxwell-Boltzmann distributed at all times. This assumption does not and should not be expected to hold, as the dark matter departs from equilibrium while transferring energy and momentum to the gas. However, for many choices of the test setup, we find that the dark matter velocity distribution does not stray too far from a thermal distribution, and so its behavior agrees well with the Maxwell-Boltzmann calculation. For other setups where the dark matter evolution departs substantially from a thermal distribution, we cannot directly predict the evolution of the system, but we still verify that the two species equilibrate sensibly and that momentum and energy are conserved. A detailed discussion of our test choices, the comparison to the naïve Maxwell-Boltzmann prediction, and the results of our simulations are given in Appendix F.

Coincidentally, our test setup is almost identical to the one employed in M. S. Fischer et al. (2025), so we re-create the most analogous of their tests (detailed in their Section 3.4). Our code produces essentially indistinguishable behavior to what they report.

4. GALAXY SIMULATIONS

As an initial application of our code to a physical system, we simulate an isolated, $z \sim 1$ Milky Way-like

galaxy, composed of an NFW profile dark matter halo of virial mass around $10^{12} M_\odot$, an exponential disk of both stars and gas, and a Hernquist profile stellar bulge. The initial conditions we use are taken from the AGORA isolated disk galaxy test (J.-h. Kim et al. 2016), where the detailed parameters are presented and explained; we give a summary in Table 1.

With these initial conditions, we perform a suite of simulations using our modified version of GIZMO (P. F. Hopkins 2015) to include dark matter–baryon interactions. We choose a dark matter particle mass of $m_\chi = 2m_p$ and velocity-independent cross sections ($n = 0$) of $\{0, 10, 30, 100, 300, 1000\} \text{ mb}$. We match the parameters and physics used in J.-h. Kim et al. (2016), including radiative cooling via the Grackle library (B. D. Smith et al. 2017), metal production, star formation, a simple thermal stellar feedback model, a Jeans pressure floor (B. E. Robertson & A. V. Kravtsov 2008), and gravitational softening lengths of 224 pc for all particle types. For the kernel used, gravity is exactly Newtonian at distances greater than 1/2.8 times the softening length (80 pc in this case).

Additionally, we use adaptive softening lengths for the gas. For dark matter, we follow the SIDM implementation in GIZMO (M. Rocha et al. 2013), which uses adaptive softening lengths *only* for determining which particles overlap and calculating the overlap integral g_{ij} . These adaptive softening lengths are initialized to 224 pc, and can vary down to a minimum of 20% of this value (44.8 pc). Importantly, the gravity solver uses fixed softening lengths for dark matter. In preliminary tests, we saw little change when instead using fixed dark matter softening lengths to compute the overlap integral.

We evolve the simulations for approximately 1 Gyr. Since we do not attempt to simulate the cosmic baryon cycle, some of the gas in the galaxy is consumed by star formation, which prematurely slows the dark matter–baryon interactions and therefore sets a limit on the length of the simulation. While longer simulations would be interesting, especially for smaller cross sections where the impact of interactions takes longer to build up, these would require a model for gas accretion during the evolution of the galaxy.

4.1. Impacts on morphology

The primary effect of the dark matter–baryon interactions is the accumulation of both gas and dark matter in the galaxy center when the cross section is large. This increased density can be seen by eye in the gas and stellar disk, which are shown face-on at a few times during the simulations in Figure 2. The gas within the central $\sim 2 \text{ kpc}$ is shown on the left; the entire stellar disk

Halo (NFW)			Disk (exponential)		
Virial mass	M_{200}	$1.074 \times 10^{12} M_{\odot}$	Mass	M_d	$4.297 \times 10^{10} M_{\odot}$
Virial radius	R_{200}	205.5 kpc	Scale length	r_d	3.432 kpc
Circular velocity	$v_{c,200}$	150 km/s	Scale height	z_d	0.3432 kpc
Concentration	c	10	Gas fraction	f_{gas}	0.2
Spin parameter	λ	0.04	Gas temperature		10^4 K
Particles	N_h	10^5	Gas metal fraction		0.02041
Stellar bulge (Hernquist)			Stellar particles	$N_{d,*}$	10^5
Mass	M_b	$4.297 \times 10^9 M_{\odot}$	Gas particles	$N_{d,\text{gas}}$	10^5
Particles	N_b	1.25×10^4			

Table 1. Parameters describing the galaxy initial conditions, from J.-h. Kim et al. (2016).

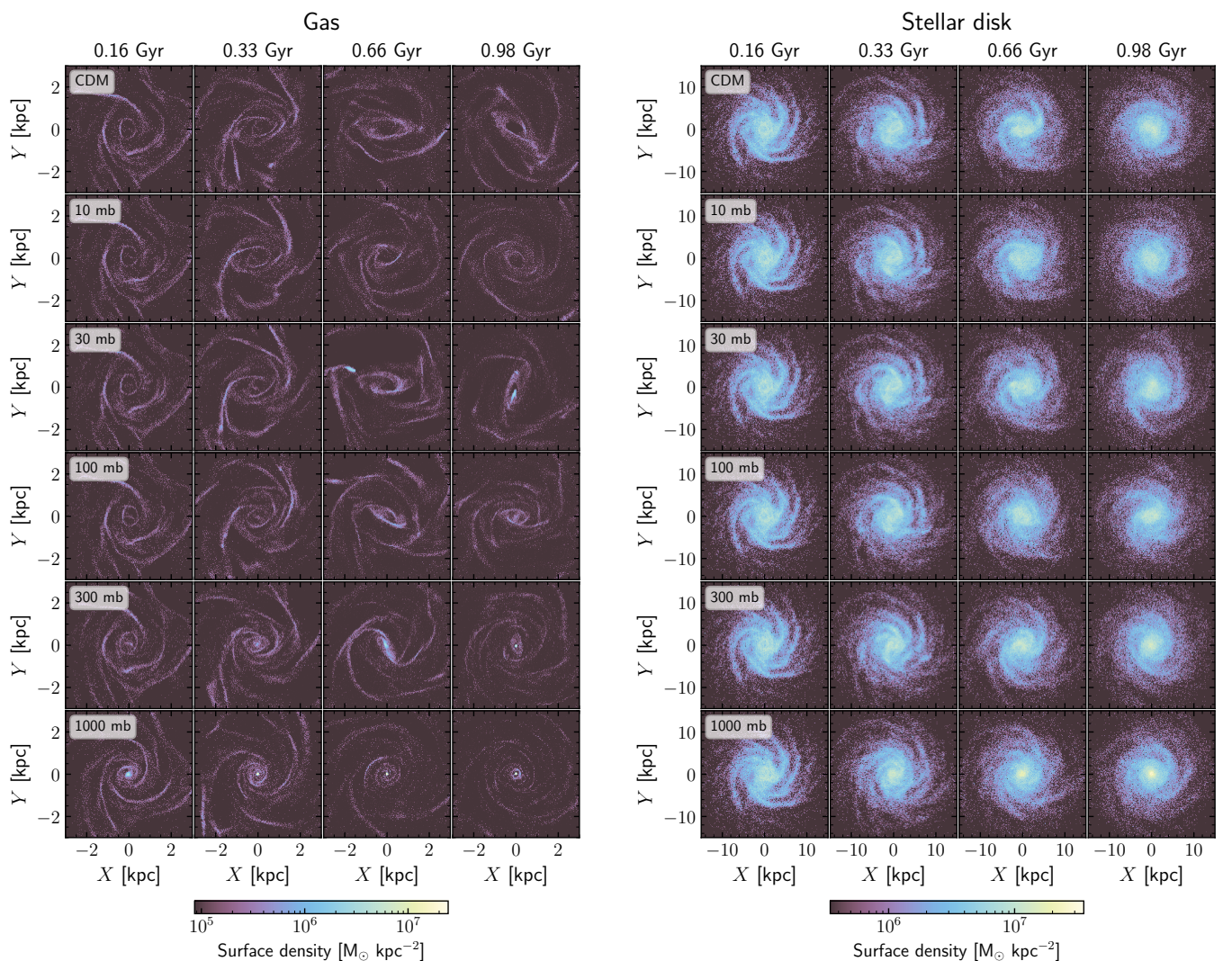


Figure 2. Top-down view of the gas in the center of the disk (left) and the entire stellar disk (right) at a variety of cross sections (increasing from top to bottom) and times (increasing from left to right). The two largest cross sections show the development of an extremely compact and dense object in the central gas, as well as the concentration of stars in the center. No significant differences are seen between CDM and the smaller cross sections.

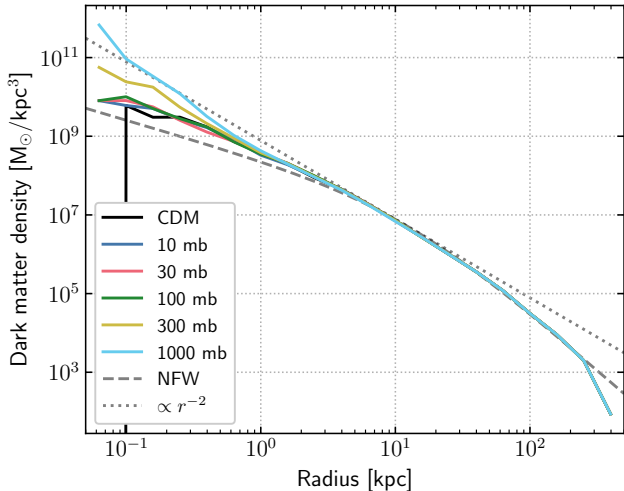


Figure 3. Dark matter density profile at the end of the simulations (at about 1 Gyr). Plotted for reference are an NFW profile chosen to match the initial conditions (dashed grey line) and a profile proportional to r^{-2} (dotted grey line). The largest two cross sections (300 and 1000 mb) are much denser in the center than all other simulations, with 1000 mb becoming steeper even than r^{-2} .

is shown on the right. Each subfigure shows a grid of images, with the cross section increasing from top to bottom and the time increasing from left to right.

The largest cross sections (300, 1000 mb) show that a considerable amount of gas falls into the center, forming an extremely compact and dense central disk of size ~ 50 pc. Because this size is approximately the minimum allowed softening length for gas particles and because we use a Jeans pressure floor, higher resolution is required to resolve the structure in the center. For 1000 mb, this process starts sooner and proceeds more quickly, eventually leading to the development of a small ring around the center with a radius of a few hundred pc. The stellar disk also concentrates in the innermost ~ 1 –2 kpc; because stars are collisionless, their response demonstrates that the potential changes drastically. Smaller cross sections show no significant differences from CDM.

The accumulation of dark matter into the center can be seen in the final dark matter density profile, plotted in Figure 3. To facilitate comparison, an NFW profile and a line with slope r^{-2} are shown as well. All profiles are approximately the same for radii outside ~ 5 kpc and closely follow the NFW profile. The 300 and 1000 mb simulations show increases in the central density as well as a steepening of the central profile. In particular, the 1000 mb simulation appears to steepen beyond r^{-2} in the center. For cross sections below 300 mb, we see no significant differences from the CDM simulation.

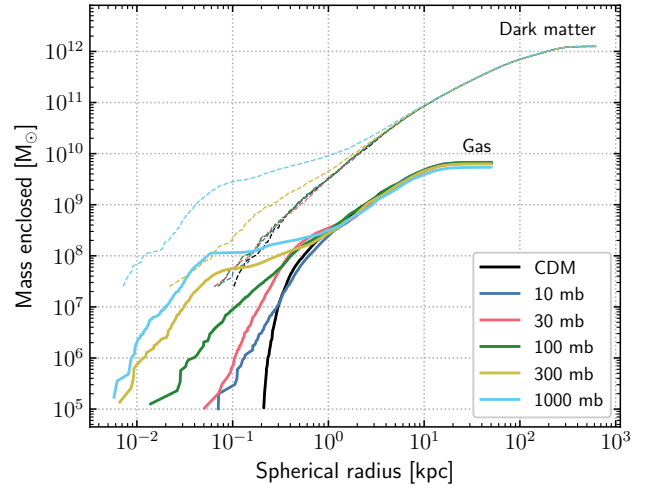


Figure 4. Enclosed dark matter (dashed) and gas (solid) mass profiles at the end of the simulations (at about 1 Gyr). Gas appears to concentrate in the center, with density increasing as a function of cross section. At the largest cross sections (300, 1000 mb), dark matter concentrates in the center as well.

The concentrations of gas and dark matter into the center can also be compared by looking at their enclosed mass profiles, which are shown in Figure 4. All gas profiles are roughly the same outside a radius of about 1 kpc; all dark matter profiles appear the same outside of about 5 kpc. But for the highest cross sections, the gas is concentrated at small radius and surrounded by a cavity of around 1 kpc in size, as seen in the face-on visualizations of Figure 2. This concentration of baryons is mirrored in the dark matter profiles. We investigate possible mechanisms driving these inflows—bar formation and transfer of angular momentum between the gas and dark matter—in Sections 4.3 and 4.4.

4.2. Impacts on gas and stars

Another quantity of interest is the temperature profile of the gas disk. For the final snapshot of each simulation, we compute the median gas temperature in 1 kpc bins of cylindrical radius up to $R = 15$ kpc; the temperature profile is shown in Figure 5. We see no significant differences at small cross sections. With the 1000 mb simulation, however, the gas temperature is increased by a significant amount at most radii. This is expected: in a Milky Way-like galaxy, the dark matter velocity dispersion is of order a few hundred km/s, which translates to an effective temperature of $\mathcal{O}(10^6$ K) for $m_\chi = 2m_p$. Hence, the dark matter is “hotter” than the gas and therefore heats it for sufficiently strong interactions.

Because dark matter–baryon interactions both heat the gas and change its density, the effects on the star

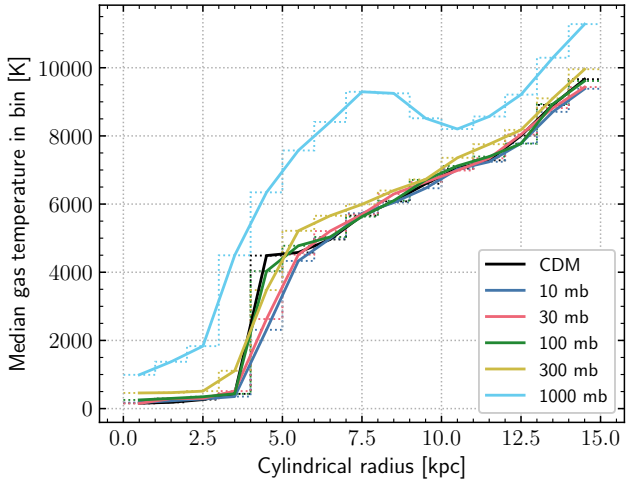


Figure 5. The median gas temperature at the end of the simulations, computed in 1 kpc bins of cylindrical radius. For a cross section of 1000 mb, there is a significant temperature increase at all radii, but the effect is largely gone for cross sections below 300 mb.

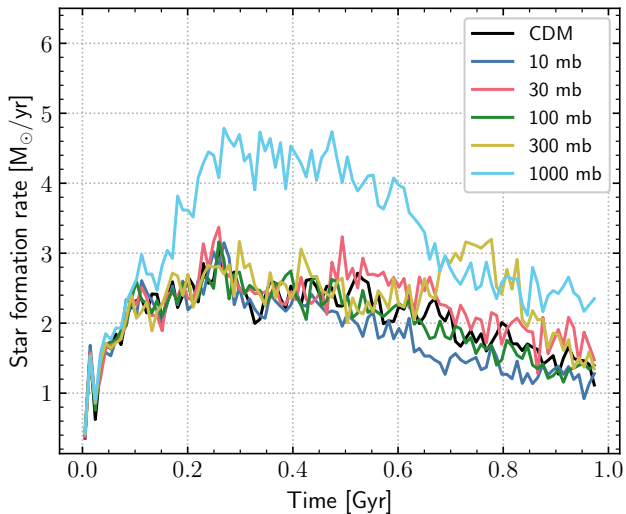


Figure 6. Star formation rate over 1 Gyr for all simulated cross sections. For a cross section of 1000 mb, the star formation rate is increased at nearly all times. At other cross sections, there are few significant differences.

formation history of the galaxy may be non-trivial. To investigate that, for each snapshot we track the total mass in newly formed stars, and take the change in stellar mass divided by the time interval between snapshots as an estimate of the star formation rate. Figure 6 shows the evolution of the star formation rate over the history of the simulation. With 1000 mb, we see enhanced star formation rates starting almost immediately, despite the elevated gas temperature. At 300 mb, the star formation rate shows few differences from CDM until around

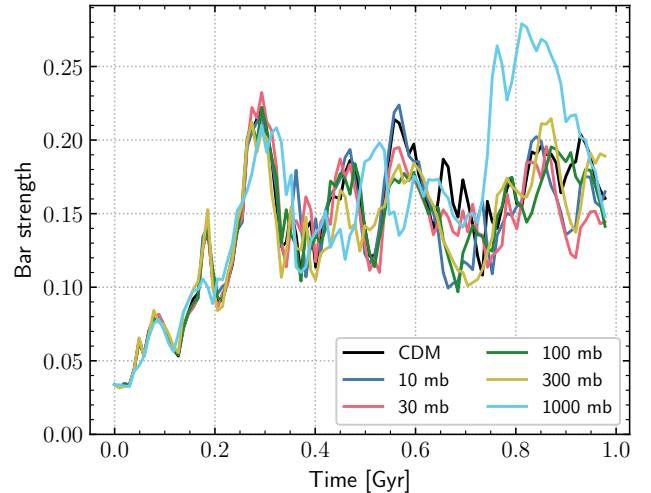


Figure 7. Bar strength of the stellar disk as a function of time. The bar strength is computed as the maximum of the second Fourier mode (Equation 21) over 1 kpc bins of cylindrical radius spanning $R \in [0, 15]$ kpc. A strength of 0.2 is a strong indicator of bar formation.

600 Myr, at which point there is a burst of increased star formation. At smaller cross sections, there are only small deviations from CDM that are uncorrelated with cross section, and so are likely just stochastic noise.

4.3. Possible role of bar formation

Because bar formation is known to drive gas inflows toward the galaxy center (R. Fanali et al. 2015), it is important that we disentangle whether dark matter–baryon interactions or a possible bar is responsible for the increased concentration discussed in Section 4.1. To this end, we investigate whether a bar forms in this simulation. The strength of a bar can be quantified using the second Fourier mode:

$$b = \frac{|\sum_j M_j \exp(2i\varphi_j)|}{\sum_j M_j}, \quad (21)$$

where M_j is the mass of star particle j and φ_j is its azimuthal angle (A. Beane et al. 2023). For every snapshot of the simulations, we compute the bar strength b in 1 kpc bins of cylindrical radius up to $R = 15$ kpc and record the maximum over the bins. Figure 7 shows the bar strength as a function of time, revealing that it evolves almost identically across all cross sections, reaching values above 0.2—a strong indicator for bar formation—within 300 Myr. In particular, during this initial period of bar formation, we find no dependence of either the bar strength or the speed of bar formation on cross section for these initial conditions.

Having convinced ourselves that formation of the bar is not affected by the presence or absence of dark

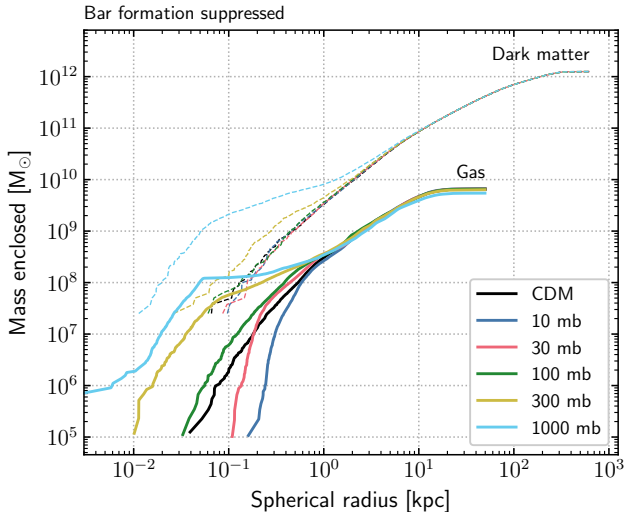


Figure 8. Enclosed dark matter (dashed) and gas (solid) mass profiles at the end of simulations with the stellar disk frozen in order to prevent bar formation. These simulations behave similarly to the simulations with bar formation, indicating that the inflow of gas and dark matter to the galaxy center is not the result of bar formation.

matter–baryon interactions, we next isolate the dark matter–baryon effects from bar-driven inflows. To do this, we perform a set of simulations with the stellar disk frozen in place; since the stars do not move, they cannot form a bar. The enclosed mass profiles of the end states of these simulations are shown in Figure 8. The results are very similar to the simulations with bar formation, indicating that dark matter–baryon interactions, and not bar formation, are driving gas and dark matter toward the center in this simulation. We emphasize that this does not mean that dark matter–baryon interactions have no effect on bar formation, and we consider this an interesting question that merits future study.

4.4. Angular momentum

The angular momentum of the gas disk (in particular, its z -component) may play a role in the development of gas inflows. Dark matter–baryon interactions introduce a new possible mechanism for transferring angular momentum into or out of the gas disk. To explore this, we investigate the evolution of the z -component of the angular momentum during these simulations. Because the dark matter at large radii in general dominates the total angular momentum, we focus on the particles in the innermost 15 kpc. The evolution of the total angular momentum of each component in this region is shown in Figure 9. We see that at large cross section (1000 mb) the dark matter gains angular momentum relative to the CDM simulation, while the gas and newly formed

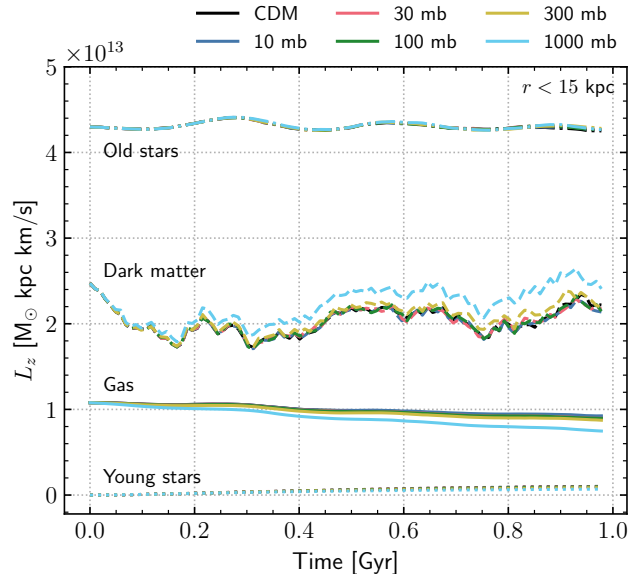


Figure 9. Evolution of the z -component of the total angular momentum for particles in the innermost 15 kpc of the galaxy. “Old stars” denote the stellar disk and bulge that are part of the initial conditions; “young stars” denote those that are formed out of the gas during the simulation. At large cross sections, the dark matter gains angular momentum relative to the CDM simulation, while the gas and young stars lose angular momentum. No significant differences are seen between CDM and the smaller cross sections.

stars lose angular momentum, providing evidence that DM–b interactions are facilitating a transfer of angular momentum.

In a galaxy simulation, one cannot directly test for conservation of energy when using dissipative physics like radiative cooling. However, angular momentum is conserved up to errors from the tree gravity solver, which gives us a useful diagnostic for whether our treatment of the dark matter–baryon interactions has introduced a source of non-conservation. For each snapshot of our simulations, we compute the total angular momentum $\mathbf{L} = \sum_i M_i \mathbf{r}_i \times \mathbf{v}_i$ and evaluate how the magnitude of this vector evolves. The evolution is shown in Figure 10, revealing that there is a non-zero but small accumulation of angular momentum during the simulation across cross sections: about 0.03% per Gyr, even with dark matter–baryon interactions disabled, or about double that for the 1000 mb case. Some small angular momentum non-conservation may be expected due to the finite separation between macroparticles at the time of interactions (as is true for SIDM implementations, see [S. Tulin & H.-B. Yu 2018](#)), which would naturally be greater with large cross sections due to the increased number of scatterings. However, since there is some accumulation in the CDM simulation, it is not clear how

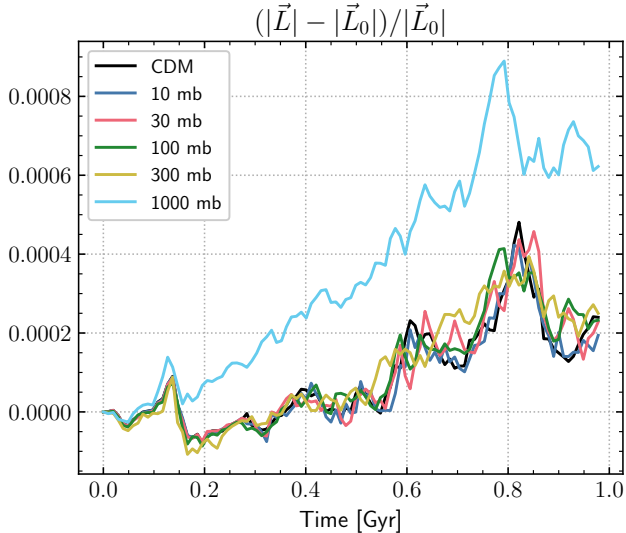


Figure 10. Fractional change in the magnitude of the total angular momentum \mathbf{L} as a function of time. At all cross sections except 1000 mb, we see extremely similar evolution, accumulating about 0.03% additional angular momentum during the simulation, indicating that there is some conservation error as a baseline. At 1000 mb, the accumulation is about twice as large, although it is not clear whether this is due to the implementation or due to the same errors simply exacerbated by the more extreme morphology of the galaxy that develops.

much of the increase at 1000 mb should be attributed to our implementation versus the errors of the tree gravity solver in the strongly reshaped galaxy, which has a more extreme morphology.

5. SUMMARY AND CONCLUSIONS

We have developed a method for incorporating dark matter–baryon interactions in cosmological N -body simulations that is accurate even in the challenging domain of dark matter with mass comparable to or lower than that of the baryon. We have implemented the method for isotropic power-law cross sections of the form $\sigma = \sigma_0 (v/c)^n$, in the simulation code GIZMO (P. F. Hopkins 2015). Our implementation is open-source, released under the GNU General Public License, and available on GitHub.¹⁰ We tested the accuracy of the model in a range of environments, including one test that is reproduced from M. S. Fischer et al. (2025) where it gives virtually identical behavior.

We have applied our implementation to the evolution of an isolated Milky Way-like disk galaxy, using initial conditions from the AGORA project (J.-h. Kim et al.

2016) and simulating the system for 1 Gyr. We considered a dark matter particle of mass $2 m_p$ with isotropic, velocity-independent DM–b cross sections of 0, 10, 30, 100, 300, and 1000 mb. For the cases of 300 and 1000 mb, the DM–b interactions clearly change the mass distribution in the central kiloparsec of the galaxy, significantly increasing the concentration of baryons and dark matter. This occurs both with and without bar formation. Interactions at this strength also heat the gas, increase the star formation rate, and facilitate the transfer of angular momentum out of the gas disk.

In our simulations with cross sections of 100 mb and less, the DM–b interactions do not have enough time to have any significant impact. This is not surprising, since the initial gas supply is partially used up, and we do not simulate gas accretion into the galaxy. Properly simulating the effect of a DM–b cross section of order 10 mb or less demands the use of high-quality hydrodynamics, modeling gas accretion, and the detailed study of the fidelity of the subgrid models of stellar feedback. These efforts are not justified in this exploratory investigation of an idealized, isolated galaxy. In future work, we plan to study cosmological galaxy formation in the interesting cross section range, with the required sophisticated treatment of the “gastrophysics”.

The code and method we have developed and presented here to incorporate dark matter–baryon interactions provide a practical, efficient, and reliable tool for the community. It should enable robust limits to be placed on various scenarios for dark matter–baryon interactions based on properties of galaxies.

ACKNOWLEDGMENTS

We thank Michael Blanton, Shy Genel, Chris Hayward, David W. Hogg, Clark Miyamoto, and Ben Wandelt for helpful discussions. We thank Moritz Fischer for his helpful feedback on our discussion of the method he and his co-authors developed. We especially thank Angus Beane for his advice and debugging aid, and Phil Hopkins for illuminating conversations about GIZMO and the possibilities for implementing this new feature. CH is supported by the National Science Foundation Graduate Research Fellowship under Grant Number DGE-2234660. This research of GRF was supported in part by the Simons Foundation. This work made use of New York University IT High Performance Computing resources, services, and staff expertise.

¹⁰ <https://github.com/cmhainje/gizmo-public>

REFERENCES

- Aalbers, J., Akerib, D. S., Musalhi, A. K. A., et al. 2025, *PhRvL*, 135, 011802, doi: [10.1103/4dyc-z8zf](https://doi.org/10.1103/4dyc-z8zf)
- Adhikari, S., Banerjee, A., Boddy, K. K., et al. 2025, *Reviews of Modern Physics*, 97, 045004, doi: [10.1103/m2vm-59y3](https://doi.org/10.1103/m2vm-59y3)
- Albakry, M. F., et al. 2023, *Phys. Rev. D*, 107, 112013, doi: [10.1103/PhysRevD.107.112013](https://doi.org/10.1103/PhysRevD.107.112013)
- Ali-Haïmoud, Y. 2019, *Phys. Rev. D*, 99, 023523, doi: [10.1103/PhysRevD.99.023523](https://doi.org/10.1103/PhysRevD.99.023523)
- Ali-Haïmoud, Y., Seher Gandhi, S., & Smith, T. L. 2024, *PhRvD*, 109, 083523, doi: [10.1103/PhysRevD.109.083523](https://doi.org/10.1103/PhysRevD.109.083523)
- Alvey, J., Bringmann, T., & Kolesova, H. 2023, *JHEP*, 01, 123, doi: [10.1007/JHEP01\(2023\)123](https://doi.org/10.1007/JHEP01(2023)123)
- Aprile, E., Abe, K., Agostini, F., et al. 2023, *PhRvL*, 131, 041003, doi: [10.1103/PhysRevLett.131.041003](https://doi.org/10.1103/PhysRevLett.131.041003)
- Beane, A., Hernquist, L., D’Onghia, E., et al. 2023, *ApJ*, 953, 173, doi: [10.3847/1538-4357/ace2b9](https://doi.org/10.3847/1538-4357/ace2b9)
- Boddy, K. K., & Gluscevic, V. 2018, *Physical Review D*, 98, 083510, doi: [10.1103/PhysRevD.98.083510](https://doi.org/10.1103/PhysRevD.98.083510)
- Boddy, K. K., Gluscevic, V., Poulin, V., et al. 2018, *Physical Review D*, 98, 123506, doi: [10.1103/PhysRevD.98.123506](https://doi.org/10.1103/PhysRevD.98.123506)
- Buen-Abad, M. A., Essig, R., McKeen, D., & Zhong, Y.-M. 2022, *Physics Reports*, 961, 1, doi: [10.1016/j.physrep.2022.02.006](https://doi.org/10.1016/j.physrep.2022.02.006)
- Bullock, J. S., & Boylan-Kolchin, M. 2017, *ARA&A*, 55, 343, doi: [10.1146/annurev-astro-091916-055313](https://doi.org/10.1146/annurev-astro-091916-055313)
- DLMF. 2025, *NIST Digital Library of Mathematical Functions*, <https://dlmf.nist.gov/>, Release 1.2.5 of 2025-12-15 <https://dlmf.nist.gov/>
- Dvorkin, C., Blum, K., & Kamionkowski, M. 2014, *Physical Review D*, 89, 023519, doi: [10.1103/PhysRevD.89.023519](https://doi.org/10.1103/PhysRevD.89.023519)
- Fanali, R., Dotti, M., Fiacconi, D., & Haardt, F. 2015, *MNRAS*, 454, 3641, doi: [10.1093/mnras/stv2247](https://doi.org/10.1093/mnras/stv2247)
- Farrar, G. R. 2022, arXiv e-prints, arXiv:2201.01334, doi: [10.48550/arXiv.2201.01334](https://doi.org/10.48550/arXiv.2201.01334)
- Fischer, M. S., Dolag, K., Garny, M., et al. 2025, *Astronomy & Astrophysics*, 700, A145, doi: [10.1051/0004-6361/202554983](https://doi.org/10.1051/0004-6361/202554983)
- Gluscevic, V., & Boddy, K. K. 2018, *Physical Review Letters*, 121, 081301, doi: [10.1103/PhysRevLett.121.081301](https://doi.org/10.1103/PhysRevLett.121.081301)
- He, A., Ivanov, M. M., An, R., Driskell, T., & Gluscevic, V. 2025, *JCAP*, 2025, 087, doi: [10.1088/1475-7516/2025/05/087](https://doi.org/10.1088/1475-7516/2025/05/087)
- He, A., Ivanov, M. M., An, R., & Gluscevic, V. 2023, *ApJL*, 954, L8, doi: [10.3847/2041-8213/acdb63](https://doi.org/10.3847/2041-8213/acdb63)
- Hopkins, P. F. 2015, *MNRAS*, 450, 53, doi: [10.1093/mnras/stv195](https://doi.org/10.1093/mnras/stv195)
- Hopkins, P. F., Wetzell, A., Kereš, D., et al. 2018, *MNRAS*, 480, 800, doi: [10.1093/mnras/sty1690](https://doi.org/10.1093/mnras/sty1690)
- Jarque, C. M., & Bera, A. K. 1980, *Economics letters*, 6, 255
- Kaplinghat, M., Ren, T., & Yu, H.-B. 2020, *JCAP*, 2020, 027, doi: [10.1088/1475-7516/2020/06/027](https://doi.org/10.1088/1475-7516/2020/06/027)
- Kim, J.-h., Agertz, O., Teyssier, R., et al. 2016, *ApJ*, 833, 202, doi: [10.3847/1538-4357/833/2/202](https://doi.org/10.3847/1538-4357/833/2/202)
- Maamari, K., Gluscevic, V., Boddy, K. K., Nadler, E. O., & Wechsler, R. H. 2021, *ApJL*, 907, L46, doi: [10.3847/2041-8213/abd807](https://doi.org/10.3847/2041-8213/abd807)
- Monaghan, J. J. 1992, *ARA&A*, 30, 543, doi: [10.1146/annurev-aa.30.090192.002551](https://doi.org/10.1146/annurev-aa.30.090192.002551)
- Moore, M., & Profumo, S. 2025, <https://arxiv.org/abs/2512.14838>
- Nadler, E. O., Drlica-Wagner, A., Bechtol, K., et al. 2021, *Physical Review Letters*, 126, 091101, doi: [10.1103/PhysRevLett.126.091101](https://doi.org/10.1103/PhysRevLett.126.091101)
- Nelson, D., Pillepich, A., Ayromlou, M., et al. 2024, *A&A*, 686, A157, doi: [10.1051/0004-6361/202348608](https://doi.org/10.1051/0004-6361/202348608)
- Nelson, D., Springel, V., Pillepich, A., et al. 2019, *Computational Astrophysics and Cosmology*, 6, 2, doi: [10.1186/s40668-019-0028-x](https://doi.org/10.1186/s40668-019-0028-x)
- Planck Collaboration, Aghanim, N., Akrami, Y., et al. 2020, *A&A*, 641, A6, doi: [10.1051/0004-6361/201833910](https://doi.org/10.1051/0004-6361/201833910)
- Robertson, B. E., & Kravtsov, A. V. 2008, *ApJ*, 680, 1083, doi: [10.1086/587796](https://doi.org/10.1086/587796)
- Rocha, M., Peter, A. H. G., Bullock, J. S., et al. 2013, *MNRAS*, 430, 81, doi: [10.1093/mnras/sts514](https://doi.org/10.1093/mnras/sts514)
- Smith, B. D., Bryan, G. L., Glover, S. C. O., et al. 2017, *MNRAS*, 466, 2217, doi: [10.1093/mnras/stw3291](https://doi.org/10.1093/mnras/stw3291)
- Spergel, D. N., & Steinhardt, P. J. 2000, *PhRvL*, 84, 3760, doi: [10.1103/PhysRevLett.84.3760](https://doi.org/10.1103/PhysRevLett.84.3760)
- Springel, V. 2005, *MNRAS*, 364, 1105, doi: [10.1111/j.1365-2966.2005.09655.x](https://doi.org/10.1111/j.1365-2966.2005.09655.x)
- Springel, V. 2010, *MNRAS*, 401, 791, doi: [10.1111/j.1365-2966.2009.15715.x](https://doi.org/10.1111/j.1365-2966.2009.15715.x)
- Tulin, S., & Yu, H.-B. 2018, *PhR*, 730, 1, doi: [10.1016/j.physrep.2017.11.004](https://doi.org/10.1016/j.physrep.2017.11.004)
- Wadekar, D., & Farrar, G. R. 2021, *Phys. Rev. D*, 103, 123028, doi: [10.1103/PhysRevD.103.123028](https://doi.org/10.1103/PhysRevD.103.123028)
- Xu, W. L., Dvorkin, C., & Chael, A. 2018, *Physical Review D*, 97, 103530, doi: [10.1103/PhysRevD.97.103530](https://doi.org/10.1103/PhysRevD.97.103530)
- Xu, X., & Farrar, G. R. 2023, *Phys. Rev. D*, 107, 095028, doi: [10.1103/PhysRevD.107.095028](https://doi.org/10.1103/PhysRevD.107.095028)

APPENDIX

A. DERIVATION OF DARK MATTER EVOLUTION

We begin with the Boltzmann equation for dark matter particle i . As written in Equation 8, the single-particle DF satisfies

$$\frac{df_{\chi}^i}{dt}(\mathbf{v}_{\chi}) = \int d^3v_B d\Omega \frac{d\sigma}{d\Omega} v_{\chi B} [f_{\chi}^i(\mathbf{S}_{\chi}) \hat{f}_B(\mathbf{S}_B) - f_{\chi}^i(\mathbf{v}_{\chi}) \hat{f}_B(\mathbf{v}_B)]. \quad (\text{A1})$$

The Boltzmann equation is made of the difference of two rates: the rate of scatters *into* a state with velocity \mathbf{v}_{χ} and the rate of scatters *out of* velocity \mathbf{v}_{χ} . The rate of scatters “in” can be conveniently reformulated by instead integrating over all possible initial velocities $\mathbf{v}'_{\chi}, \mathbf{v}'_B$ and scattering angles Ω , conditioned on the requirement that the post-scatter velocity is \mathbf{v}_{χ} :

$$\frac{df_{\chi}^i}{dt}(\mathbf{v}_{\chi}) = \int d^3v'_{\chi} d^3v'_B d\Omega \frac{d\sigma}{d\Omega} v_{\chi' B'} f_{\chi}^i(\mathbf{v}'_{\chi}) \hat{f}_B(\mathbf{v}'_B) \delta(\mathbf{S}_{\chi}(\mathbf{v}'_{\chi}) - \mathbf{v}_{\chi}) - \int d^3v_B d\Omega \frac{d\sigma}{d\Omega} v_{\chi B} f_{\chi}^i(\mathbf{v}_{\chi}) \hat{f}_B(\mathbf{v}_B). \quad (\text{A2})$$

We will primarily use this form of the Boltzmann equation in the following derivations.

Consider the evolution of this single-particle DF over a timestep Δt . To first order in the timestep, the update is

$$f_{\chi}^i \Big|_{t+\Delta t} = f_{\chi}^i \Big|_t + \frac{df_{\chi}^i}{dt} \Big|_t \Delta t. \quad (\text{A3})$$

The updated DF has the form $n_i(\mathbf{x}) \nu'_i(\mathbf{v})$, where ν'_i is the new velocity distribution of the particle. Plugging in \hat{f}_B , we thus find

$$n_i(\mathbf{x}) \nu'_i(\mathbf{v}) = n_i(\mathbf{x}) \left[\left(1 - \sum_j n_j(\mathbf{x}) \int d^3v_B d\Omega \mathcal{G}(\mathbf{v}_B - \mathbf{V}_j, T_j/\mu_j) \frac{d\sigma}{d\Omega} v_{iB} \Delta t \right) \delta(\mathbf{v} - \mathbf{v}_i) + \sum_j n_j(\mathbf{x}) \int d^3v_B d\Omega \mathcal{G}(\mathbf{v}_B - \mathbf{V}_j, T_j/\mu_j) \frac{d\sigma}{d\Omega} v_{iB} \Delta t \delta(\mathbf{v} - \mathbf{S}_{\chi}(\mathbf{v}_i)) \right]. \quad (\text{A4})$$

The result contains two integrals over d^3v_B for each gas particle j . The second is tricky, as the integration variables \mathbf{v}_B and Ω are used in the scattering transformation \mathbf{S}_{χ} inside the Dirac delta function. Therefore, it is expedient to approximate the integrals instead by Monte Carlo sampling. The integrals can be performed independently for each particle j using single samples from the baryon Maxwell-Boltzmann distribution, which we denote \mathbf{v}_{ij}^B , and the angular component of the differential cross section, Ω_{ij} . The result is

$$n_i(\mathbf{x}) \nu'_i(\mathbf{v}) = n_i(\mathbf{x}) \left[\left(1 - \sum_j n_j(\mathbf{x}) \sigma(v_{\text{rel}}) v_{\text{rel}} \Delta t \right) \delta(\mathbf{v} - \mathbf{v}_i) + \sum_j n_j(\mathbf{x}) \sigma(v_{\text{rel}}) v_{\text{rel}} \Delta t \delta(\mathbf{v} - \mathbf{S}_{\chi}(\mathbf{v}_i; \mathbf{v}_{ij}^B, \Omega_{ij})) \right], \quad (\text{A5})$$

where $v_{\text{rel}} \equiv |\mathbf{v}_i - \mathbf{v}_{ij}^B|$, and $\sigma(v)$ is the total cross section, given by $\sigma(v) = \int d\Omega (d\sigma/d\Omega)|_v$. The total cross section appears because one can decompose the differential cross section as

$$\frac{d\sigma}{d\Omega} \Big|_{v, \Omega} = \sigma(v) p(\Omega | v), \quad (\text{A6})$$

where $p(\Omega | v)$ is the probability density of scattering angles conditioned on the relative velocity. The sample Ω_{ij} is drawn from $p(\Omega | v_{\text{rel}})$, allowing us to approximate $d\sigma/d\Omega \approx \sigma(v) \delta(\Omega - \Omega_{ij})$, and the rest follows.

In order to isolate $\nu'_i(\mathbf{v})$ from all \mathbf{x} dependence, we can integrate both sides over all space. We find

$$\nu'_i(\mathbf{v}) = \left(1 - \sum_j P_{ij} \right) \delta(\mathbf{v} - \mathbf{v}_i) + \sum_j P_{ij} \delta(\mathbf{v} - \mathbf{S}_{\chi}(\mathbf{v}_i, \mathbf{v}_{ij}^B, \Omega_{ij})), \quad (\text{A7})$$

where we have introduced

$$g_{ij} \equiv \int d^3x W(|\mathbf{x} - \mathbf{x}_i|, h_i) W(|\mathbf{x} - \mathbf{x}_j|, h_j) \quad \text{and} \quad P_{ij} \equiv \frac{M_j}{\mu_j} g_{ij} \sigma(v_{\text{rel}}) v_{\text{rel}} \Delta t. \quad (\text{A8})$$

B. DERIVATION OF BARYON EVOLUTION

Because the baryons are assumed to thermalize on timescales faster than the timesteps of the simulation, we impose that the baryon velocity distribution is at all times Maxwell-Boltzmann. Thus, the evolution of gas particle j is described by the rates-of-change of the bulk velocity and temperature:

$$n_j(\mathbf{x}) \frac{d\mathbf{V}_j}{dt} = \int d^3v_B \frac{df_B^j}{dt} \Big|_{\mathbf{x}, \mathbf{v}_B} \mathbf{v}_B, \quad (\text{B9})$$

$$n_j(\mathbf{x}) \frac{3}{\mu_j} \frac{dT_j}{dt} = \int d^3v_B \frac{df_B^j}{dt} \Big|_{\mathbf{x}, \mathbf{v}_B} (\mathbf{v}_B - \mathbf{V}_j)^2. \quad (\text{B10})$$

As we proceed, we will use the notation $f_\chi = f_\chi(\mathbf{x}, \mathbf{v}_\chi)$, $f'_\chi = f_\chi(\mathbf{x}, \mathbf{v}'_\chi)$, $f_B = f_B^j(\mathbf{x}, \mathbf{v}_B)$, $f'_B = f_B^j(\mathbf{x}, \mathbf{v}'_B)$. We start with the acceleration. Inserting the Boltzmann equation gives

$$\begin{aligned} n_j(\mathbf{x}) \frac{d\mathbf{V}_j}{dt} &= \int d^3v_B d^3v'_\chi d^3v'_B d\Omega f'_\chi f'_B \frac{d\sigma}{d\Omega} v_{B'\chi'} \delta(\mathbf{v}_B - \mathbf{S}(\mathbf{v}'_B)) \mathbf{v}_B \\ &\quad - \int d^3v_B d^3v_\chi d\Omega f_\chi f_B \frac{d\sigma}{d\Omega} v_{B\chi} \mathbf{v}_B. \end{aligned} \quad (\text{B11})$$

The Dirac delta function in the first integral can be integrated immediately. Then, the two terms are identical up to a relabeling of primed and unprimed velocities and the replacement of \mathbf{v}_B by $\mathbf{S}(\mathbf{v}_B)$. Using these facts, we find

$$n_j(\mathbf{x}) \frac{d\mathbf{V}_j}{dt} = \int d^3v_\chi d^3v_B d\Omega f_\chi f_B \frac{d\sigma}{d\Omega} v_{B\chi} [\mathbf{S}(\mathbf{v}_B) - \mathbf{v}_B] \quad (\text{B12})$$

$$= \int d^3v_\chi d^3v_B d\Omega f_\chi f_B \frac{d\sigma}{d\Omega} v_{B\chi}^2 \frac{m_\chi}{m_\chi + \mu_j} [\hat{\mathbf{v}}'_{B\chi} - \hat{\mathbf{v}}_{B\chi}]. \quad (\text{B13})$$

For fixed $\mathbf{v}_\chi, \mathbf{v}_B$, the integral over Ω can only result in a vector aligned with $\hat{\mathbf{v}}_{B\chi}$, so we can project these vectors along this direction. In other words, we can make the following substitution in the integrand: $\hat{\mathbf{v}}'_{B\chi} - \hat{\mathbf{v}}_{B\chi} \mapsto \hat{\mathbf{v}}_{B\chi} [\hat{\mathbf{v}}_{B\chi} \cdot \hat{\mathbf{v}}'_{B\chi} - 1]$. We now introduce the momentum transfer cross section:

$$\bar{\sigma}(v_{\text{rel}}) \equiv \int d\Omega \frac{d\sigma}{d\Omega} \Big|_{v_{\text{rel}}} [1 - \cos \theta] = \int d\Omega \frac{d\sigma}{d\Omega} \Big|_{v_{\text{rel}}} [1 - \hat{\mathbf{v}}'_{\text{rel}} \cdot \hat{\mathbf{v}}_{\text{rel}}]. \quad (\text{B14})$$

Thus,

$$n_j(\mathbf{x}) \frac{d\mathbf{V}_j}{dt} = -\frac{m_\chi}{m_\chi + \mu_j} \int d^3v_\chi d^3v_B f_\chi f_B \bar{\sigma}(v_{B\chi}) v_{B\chi} \mathbf{v}_{B\chi}. \quad (\text{B15})$$

Now we insert the Maxwell-Boltzmann form of f_B^j . Introducing $\mathbf{u} \equiv \mathbf{v}_\chi - \mathbf{v}_B$ and $\mathbf{w} \equiv \mathbf{v}_\chi - \mathbf{V}_j$, we arrive at

$$n_j(\mathbf{x}) \frac{d\mathbf{V}_j}{dt} = \frac{m_\chi}{m_\chi + \mu_j} n_j(\mathbf{x}) \int d^3v_\chi f_\chi \left[\underbrace{\int d^3u \mathcal{G}(\mathbf{w} - \mathbf{u}, T_j/\mu_j) \bar{\sigma}(u) \frac{\mathbf{u} \cdot \mathbf{w}}{w^2}}_{\equiv \mathcal{A}(\mathbf{w}; T_j/\mu_j)} \right] \mathbf{w}, \quad (\text{B16})$$

Finally we can insert the DF for the dark matter and integrate both sides over space:

$$n_j(\mathbf{x}) \frac{d\mathbf{V}_j}{dt} \approx \frac{m_\chi}{m_\chi + \mu_j} n_j(\mathbf{x}) \sum_i n_i(\mathbf{x}) \mathcal{A}(\mathbf{v}_i - \mathbf{V}_j; T_j/\mu_j) (\mathbf{v}_i - \mathbf{V}_j) \quad (\text{B17})$$

$$\implies \frac{d\mathbf{V}_j}{dt} = \sum_i \frac{M_i}{m_\chi + \mu_j} g_{ij} \mathcal{A}(\mathbf{v}_i - \mathbf{V}_j; T_j/\mu_j) (\mathbf{v}_i - \mathbf{V}_j). \quad (\text{B18})$$

The heating rate proceeds similarly. We begin by inserting the Boltzmann equation:

$$n_j(\mathbf{x}) \frac{3}{\mu_j} \frac{dT_j}{dt} = \int d^3v_B d^3v'_\chi d^3v'_B d\Omega f'_\chi f'_B \frac{d\sigma}{d\Omega} v_{B'\chi'} \delta(\mathbf{v}_B - \mathbf{S}(\mathbf{v}'_B)) (\mathbf{v}_B - \mathbf{V}_j)^2 \quad (\text{B19})$$

$$- \int d^3v_B d^3v_\chi d\Omega f_\chi f_B \frac{d\sigma}{d\Omega} v_{B\chi} (\mathbf{v}_B - \mathbf{V}_j)^2$$

$$= \int d^3v_\chi d^3v_B d\Omega f_\chi f_B \frac{d\sigma}{d\Omega} v_{B\chi} [(\mathbf{S}(\mathbf{v}_B) - \mathbf{V}_j)^2 - (\mathbf{v}_B - \mathbf{V}_j)^2] \quad (\text{B20})$$

$$= \int d^3v_\chi d^3v_B d\Omega f_\chi f_B \frac{d\sigma}{d\Omega} v_{B\chi} [(\mathbf{S}(\mathbf{v}_B) - \mathbf{v}_B)^2 + 2(\mathbf{v}_B - \mathbf{V}_j) \cdot (\mathbf{S}(\mathbf{v}_B) - \mathbf{v}_B)]. \quad (\text{B21})$$

We now split this into two terms. The first contains

$$\int d\Omega \frac{d\sigma}{d\Omega} (\mathbf{S}(\mathbf{v}_B) - \mathbf{v}_B)^2 = \left(\frac{m_\chi v_{B\chi}}{m_\chi + \mu_j} \right)^2 \int d\Omega \frac{d\sigma}{d\Omega} (\hat{v}'_{B\chi} - \hat{v}_{B\chi})^2 = 2 \left(\frac{m_\chi v_{B\chi}}{m_\chi + \mu_j} \right)^2 \bar{\sigma}(v_{B\chi}). \quad (\text{B22})$$

The second:

$$(\mathbf{v}_B - \mathbf{V}_j) \cdot \int d\Omega \frac{d\sigma}{d\Omega} (\mathbf{S}(\mathbf{v}_B) - \mathbf{v}_B) = -\frac{m_\chi}{m_\chi + \mu_j} \bar{\sigma}(v_{B\chi}) v_{B\chi} (\mathbf{v}_B - \mathbf{V}_j) \cdot \mathbf{v}_{B\chi} \quad (\text{B23})$$

$$= -\frac{m_\chi}{m_\chi + \mu_j} \bar{\sigma}(v_{B\chi}) v_{B\chi} [v_{B\chi}^2 + (\mathbf{v}_\chi - \mathbf{V}_j) \cdot \mathbf{v}_{B\chi}]. \quad (\text{B24})$$

Putting these in,

$$n_j(\mathbf{x}) \frac{3}{\mu_j} \frac{dT_j}{dt} = 2 \frac{m_\chi}{m_\chi + \mu_j} \int d^3v_\chi d^3v_B f_\chi f_B \bar{\sigma}(v_{B\chi}) \left[\frac{m_\chi}{m_\chi + \mu_j} v_{B\chi}^3 - v_{B\chi}^3 - v_{B\chi} (\mathbf{v}_\chi - \mathbf{V}_j) \cdot \mathbf{v}_{B\chi} \right] \quad (\text{B25})$$

$$= 2 \frac{m_\chi}{m_\chi + \mu_j} \int d^3v_\chi d^3v_B f_\chi f_B \bar{\sigma}(v_{B\chi}) \left[-\frac{\mu_j}{m_\chi + \mu_j} v_{B\chi}^3 - v_{B\chi} (\mathbf{v}_\chi - \mathbf{V}_j) \cdot \mathbf{v}_{B\chi} \right]. \quad (\text{B26})$$

Now, like before, we insert the Maxwell-Boltzmann form of f_B^j , change variables, and find

$$n_j(\mathbf{x}) \frac{3}{\mu_j} \frac{dT_j}{dt} = 2 \frac{m_\chi}{m_\chi + \mu_j} n_j(\mathbf{x}) \int d^3v_\chi f_\chi \left[-\frac{\mu_j}{m_\chi + \mu_j} \mathcal{B}(\mathbf{w}; T_j/\mu_j) + (\mathbf{v}_\chi - \mathbf{V}_j)^2 \mathcal{A}(\mathbf{w}; T_j/\mu_j) \right], \quad (\text{B27})$$

where we introduced

$$\mathcal{B}(\mathbf{w}; \varsigma^2) \equiv \int d^3u \mathcal{G}(\mathbf{w} - \mathbf{u}, \varsigma^2) u^3 \bar{\sigma}(u). \quad (\text{B28})$$

Finally we can insert the form of f_χ and integrate both sides over space:

$$n_j(\mathbf{x}) \frac{3}{2\mu_j} \frac{dT_j}{dt} = \frac{m_\chi}{m_\chi + \mu_j} n_j(\mathbf{x}) \sum_i n_i(\mathbf{x}) \left[(\mathbf{v}_i - \mathbf{V}_j)^2 \mathcal{A}(\mathbf{v}_i - \mathbf{V}_j; T_j/\mu_j) - \frac{\mu_j}{m_\chi + \mu_j} \mathcal{B}(\mathbf{v}_i - \mathbf{V}_j; T_j/\mu_j) \right] \quad (\text{B29})$$

$$\implies \frac{3}{2\mu_j} \frac{dT_j}{dt} = \sum_i \frac{M_i}{m_\chi + \mu_j} g_{ij} \left[(\mathbf{v}_i - \mathbf{V}_j)^2 \mathcal{A}(\mathbf{v}_i - \mathbf{V}_j; T_j/\mu_j) - \frac{\mu_j}{m_\chi + \mu_j} \mathcal{B}(\mathbf{v}_i - \mathbf{V}_j; T_j/\mu_j) \right]. \quad (\text{B30})$$

As noted by [Y. Ali-Haïmoud \(2019\)](#), \mathcal{A} and \mathcal{B} have simple forms in terms of special functions if the momentum transfer cross section has a power-law dependence on v . Specifically, if $\bar{\sigma}(v_{\text{rel}}) = \sigma_0 (v_{\text{rel}}/c)^n$ for integer $n \geq -4$, then

$$\mathcal{A}(w; \varsigma^2) = \frac{\alpha_n}{3} \frac{\sigma_0}{c^n} \varsigma^{n+1} {}_1F_1 \left(-\frac{n+1}{2}, \frac{5}{2}, -\frac{w^2}{2\varsigma^2} \right), \quad (\text{B31})$$

$$\mathcal{B}(w; \varsigma^2) = \alpha_n \frac{\sigma_0}{c^n} \varsigma^{n+3} {}_1F_1 \left(-\frac{n+3}{2}, \frac{3}{2}, -\frac{w^2}{2\varsigma^2} \right), \quad (\text{B32})$$

$$\alpha_n \equiv \frac{2^{(n+5)/2} \Gamma(3 + \frac{n}{2})}{\sqrt{\pi}}, \quad (\text{B33})$$

where ${}_1F_1$ is the confluent hypergeometric function of the first kind.

C. EQUIVALENCE OF THE TWO APPROACHES

In this appendix, we show that momentum and energy are conserved in expectation value given the two approaches, so the two approaches are statistically equivalent. For dark matter, we have in the end computed the updated velocity distribution of particle i to be

$$\nu'_i(\mathbf{v}) \Big|_{t+\Delta t} = \frac{m_\chi}{M_i} \int d^3x \left(f_\chi^i \Big|_t + \frac{df_\chi^i}{dt} \Big|_t \Delta t \right). \quad (\text{C34})$$

At the end of a timestep, we draw a sample from this distribution ν'_i , which itself involves approximating df_χ^i/dt by drawing samples from the distributions of baryon velocities and scattering angles. The average change in velocity, then, is given by integrating over all possible samples (i.e., reverting the sampling approximations):

$$\begin{aligned} \mathbb{E}[\Delta \mathbf{v}_i] &= \frac{m_\chi}{M_i} \int d^3x d^3v \left(f_\chi^i \Big|_t + \frac{df_\chi^i}{dt} \Big|_t \Delta t \right) \mathbf{v} - \mathbf{v}_i \\ &= \frac{m_\chi}{M_i} \int d^3x d^3v \frac{df_\chi^i}{dt} \Big|_t \Delta t \mathbf{v}. \end{aligned} \quad (\text{C35})$$

Notice that the integral over $(df/dt) \mathbf{v}$ is exactly how we define the mean acceleration for the baryons. One can follow the derivation of $d\mathbf{V}_j/dt$ in Appendix B line-by-line with the subscripts B and χ exchanged to obtain this expectation value; the entire derivation is symmetric. The result is

$$\mathbb{E}[\Delta \mathbf{v}_i] = \sum_j \frac{M_j}{m_\chi + \mu_j} g_{ij} \mathcal{A}(\mathbf{v}_i - \mathbf{V}_j; T_j/\mu_j) (\mathbf{V}_j - \mathbf{v}_i) \Delta t. \quad (\text{C36})$$

The change in energy can be similarly considered.

$$\mathbb{E}[\Delta E_i] = \frac{M_i}{2} \frac{m_\chi}{M_i} \int d^3x d^3v \left(f_\chi^i \Big|_t + \frac{df_\chi^i}{dt} \Big|_t \Delta t \right) \mathbf{v}^2 - \mathbf{v}_i^2 \quad (\text{C37})$$

$$= \frac{m_\chi}{2} \int d^3x d^3v \frac{df_\chi^i}{dt} \Big|_t \Delta t \mathbf{v}^2 \quad (\text{C38})$$

$$= \frac{m_\chi}{2} \int d^3x d^3v d^3v_B d\Omega f_\chi f_B \frac{d\sigma}{d\Omega} v_{\chi B} [\mathbf{S}(\mathbf{v})^2 - \mathbf{v}^2] \Delta t \quad (\text{C39})$$

$$= \frac{m_\chi}{2} \int d^3x d^3v d^3v_B d\Omega f_\chi f_B \frac{d\sigma}{d\Omega} v_{\chi B} [(\mathbf{S}(\mathbf{v}) - \mathbf{v})^2 + 2\mathbf{v} \cdot (\mathbf{S}(\mathbf{v}) - \mathbf{v})] \Delta t \quad (\text{C40})$$

$$= \frac{m_\chi \mu_j}{m_\chi + \mu_j} \int d^3x d^3v d^3v_B f_\chi f_B \bar{\sigma} \left[-\frac{m_\chi}{m_\chi + \mu_j} v_{\chi B}^3 - v_{\chi B} \mathbf{v}_B \cdot \mathbf{v}_{\chi B} \right] \Delta t \quad (\text{C41})$$

$$= \frac{m_\chi \mu_j}{m_\chi + \mu_j} \int d^3x d^3v d^3v_B f_\chi f_B \bar{\sigma} \left[\frac{\mu_j}{m_\chi + \mu_j} v_{\chi B}^3 - v_{\chi B} \mathbf{v}_\chi \cdot \mathbf{v}_{\chi B} \right] \Delta t \quad (\text{C42})$$

$$= m_\chi \sum_j \frac{M_j}{m_\chi + \mu_j} n_j(\mathbf{x}) \int d^3x d^3v f_\chi \left[\frac{\mu_j}{m_\chi + \mu_j} \mathcal{B}(\mathbf{w}; T_j/\mu_j) - \mathbf{v}_\chi \cdot (\mathbf{v}_\chi - \mathbf{V}_j) \mathcal{A}(\mathbf{w}; T_j/\mu_j) \right] \Delta t \quad (\text{C43})$$

$$= M_i \sum_j \frac{M_j}{m_\chi + \mu_j} g_{ij} \left[\frac{\mu_j}{m_\chi + \mu_j} \mathcal{B}(\mathbf{v}_i - \mathbf{V}_j; T_j/\mu_j) - \mathbf{v}_i \cdot (\mathbf{v}_i - \mathbf{V}_j) \mathcal{A}(\mathbf{v}_i - \mathbf{V}_j; T_j/\mu_j) \right] \Delta t. \quad (\text{C44})$$

Suppose we have exactly one dark matter particle i and one gas particle j . Then, the rates-of-change satisfy the following relationships:

$$M_i \mathbb{E}[\Delta \mathbf{v}_i] + M_j \frac{d\mathbf{V}_j}{dt} \Delta t = 0, \quad (\text{C45})$$

$$\mathbb{E}[\Delta E_i] + \frac{3M_j}{2\mu_j} \frac{dT_j}{dt} \Delta t + M_j \mathbf{V}_j \cdot \frac{d\mathbf{V}_j}{dt} \Delta t = 0. \quad (\text{C46})$$

These relationships are recognizable as conservation of the expectation values of energy and momentum.

As we extend to many dark matter and many gas particles, these relationships continue to hold for each individual pair. This is because both the full expectation values we have just computed *and* the baryonic rates-of-change simply sum over neighbors of the other type. Hence, for each pair (i, j) , equal and opposite terms appear in the expectation values for the change to i and in the rates-of-change of j .

D. COMPUTATION OF OVERLAP INTEGRAL

Let us consider the computation of the overlap factor g_{ij} . It is defined

$$g_{ij} \equiv \int d^3x W(|\mathbf{x} - \mathbf{x}_i|; h_i) W(|\mathbf{x} - \mathbf{x}_j|; h_j). \quad (\text{D47})$$

We assume that the gas and dark matter are softened with the same kernel W ; the transformations and tabulation described below will need to be reworked if the two use different softening kernels.

Define the distance $|\mathbf{x}_i - \mathbf{x}_j| \equiv d$. Let us translate our integration variable to place \mathbf{x}_i at the origin. The integral is invariant to rotation, so we choose to place \mathbf{x}_j at $d\hat{z}$. Then,

$$g_{ij} \equiv \int d^3x W(|\mathbf{x}|; h_i) W(|\mathbf{x} - d\hat{z}|; h_j). \quad (\text{D48})$$

We now move to spherical coordinates: $\mathbf{x} \rightarrow (r, \theta, \phi)$, so

$$g_{ij} = \int dr dc d\phi r^2 W(r; h_i) W(\sqrt{r^2 + d^2 - 2dr c}; h_j) \quad (\text{D49})$$

$$= 2\pi \int_0^{h_i} dr r^2 W(r; h_i) \int_{-1}^{+1} dc W(\sqrt{r^2 + d^2 - 2dr c}; h_j), \quad (\text{D50})$$

with $c \equiv \cos \theta$.

Generally, the softening kernel depends only on the ratio of its arguments, up to a normalizing factor in terms of h . In other words,

$$W(x; h) = \frac{1}{h^3} w(x/h), \quad (\text{D51})$$

for some w . Let $s \equiv r/h_i$ and $\delta \equiv d/h_i$. Then,

$$g_{ij} = 2\pi \int dr dc r^2 W(r; h_i) W(\sqrt{r^2 + d^2 - 2dr c}; h_j) \quad (\text{D52})$$

$$= \frac{2\pi}{h_i^3 h_j^3} \int dr dc r^2 w(r/h_i) w(\sqrt{r^2 + d^2 - 2dr c}/h_j) \quad (\text{D53})$$

$$= \frac{2\pi}{h_j^3} \int_0^1 ds s^2 w(s) \int_{-1}^{+1} dc w(\sqrt{s^2 + \delta^2 - 2\delta s c}/(h_j/h_i)). \quad (\text{D54})$$

For a given softening kernel, the integral that remains can be tabulated in terms of two parameters: δ and h_j/h_i .

Because g_{ij} is symmetric, we need only tabulate values of the ratio h_j/h_i between 0 and 1; any ratio $h_j/h_i > 1$ can be handled by swapping $i \leftrightarrow j$.

The range of δ can also be considered. We assume W is zero beyond the smoothing length, so the overlap is zero if $d > h_i + h_j$. Thus, the range of δ that gives non-zero overlap can be found:

$$d < h_i + h_j \implies \delta < 1 + \frac{h_j}{h_i}. \quad (\text{D55})$$

Since we choose i and j such that $h_j/h_i \leq 1$, δ only needs to be tabulated from 0 to 2. For small values of h_j/h_i , parts of the table will simply be zero.

We note that this method is almost the same as that described by [M. S. Fischer et al. \(2025\)](#), although we use spherical rather than cylindrical coordinates to better match the SIDM implementation in GIZMO ([M. Rocha et al. 2013](#)).

E. REGIME OF VALIDITY OF THE F25 METHOD

As discussed in Section 2.5, we have performed a numerical experiment to quantify the regions of validity of the “rare, large-angle scattering” method of M. S. Fischer et al. (2025, F25). Here we describe that experiment.

We consider two macroparticles, one dark matter and one baryon, with velocities like those of our test method (see Section 3 or the more detailed discussion below). For this single pair of macroparticles, assumed to be overlapping with some fiducial value for g_{ij} , we perform 100 000 scatterings. Each scattering involves randomly sampling a dark matter velocity from a Maxwell-Boltzmann distribution, a “virtual baryon” velocity from a Maxwell-Boltzmann distribution, and a scattering angle. We then compute the change to the bulk velocity \mathbf{V}_B and the internal specific energy U_B of the baryon according to the algorithm described in F25.

We are primarily interested in the energy transfer. We define the total specific energy of the baryon to be

$$\mathcal{E}_B = \frac{1}{2} \mathbf{V}_B^2 + U_B. \quad (\text{E56})$$

In each trial i , the scattering occurs with some probability P_i , which depends on the sampled velocities. So, the *expected* change in the total energy of the baryon for trial i is

$$\Delta \mathcal{E}_i = P_i (\mathcal{E}'_B - \mathcal{E}_B) + (1 - P_i) 0 = P_i (\mathcal{E}'_B - \mathcal{E}_B). \quad (\text{E57})$$

By averaging this quantity over many trials, we compute the expectation value of the change in energy, integrating by Monte Carlo over scattering angle and the dark matter and baryon velocity distributions:

$$\mathbb{E}[\Delta \mathcal{E}_B] = \frac{1}{N_{\text{trials}}} \sum_{i \in \text{trials}} P_i (\mathcal{E}'_B - \mathcal{E}_B). \quad (\text{E58})$$

In the F25 algorithm, a scattering is rejected if it results in negative internal energy U'_B . Hence, given all these trial scatterings, the expected change in energy that will actually result from the F25 algorithm is given by averaging over only those trials where $U'_B > 0$:

$$\mathbb{E}[\Delta \mathcal{E}_B]_{\text{actual}} = \frac{1}{N_{\text{trials}|U'_B > 0}} \sum_{i \in \text{trials}|U'_B > 0} P_i (\mathcal{E}'_B - \mathcal{E}_B). \quad (\text{E59})$$

We can also compute the expected rejection rate, which is the probability-weighted fraction of scatterings that were rejected:

$$f_{\text{reject}} = \frac{\sum_{i \in \text{trials}} P_i \mathbf{1}(U'_B \leq 0)}{\sum_{i \in \text{trials}} P_i}, \quad (\text{E60})$$

where $\mathbf{1}(\text{cond})$ is the condition function: 1 if the condition is true and 0 otherwise.

We expect the rejection rate to depend primarily on two mass ratios: that of the macroparticles M_χ/M_B and of the physical particles m_χ/m_B . We therefore conduct this experiment for a wide range of both ratios. The resulting rejection rates and energy change bias fractions (actual divided by expected) are shown as heatmaps in Figure 11. Also shown on these figures is the expected “safe zone” described in F25:

$$\frac{M_\chi}{M_B} < \frac{3}{28} \frac{m_\chi}{m_B}. \quad (\text{E61})$$

We find that the rejection rate is zero and the bias fraction is one everywhere in the expected safe zone, and even for M_χ/M_B slightly greater than the safe zone threshold. However, performance degrades steeply once $M_\chi/M_B \gtrsim m_\chi/m_B$, with the rejection rate becoming 100% almost everywhere. In general, the effect of the rejections is to reduce the number of scatters and therefore to bias the energy transfer downward, which is borne out by the observed bias ratio. In fact, for most of the mass ratios tested, the bias ratio becomes exactly zero, with energy transfer completely shut off. However, there is a small region where the rejections actually enhance the energy transfer; this is because the distribution of energy transfers is broad when the macroparticle mass ratio is similar to that of the physical particles, and the rejection step only cuts off the negative tail of the distribution.

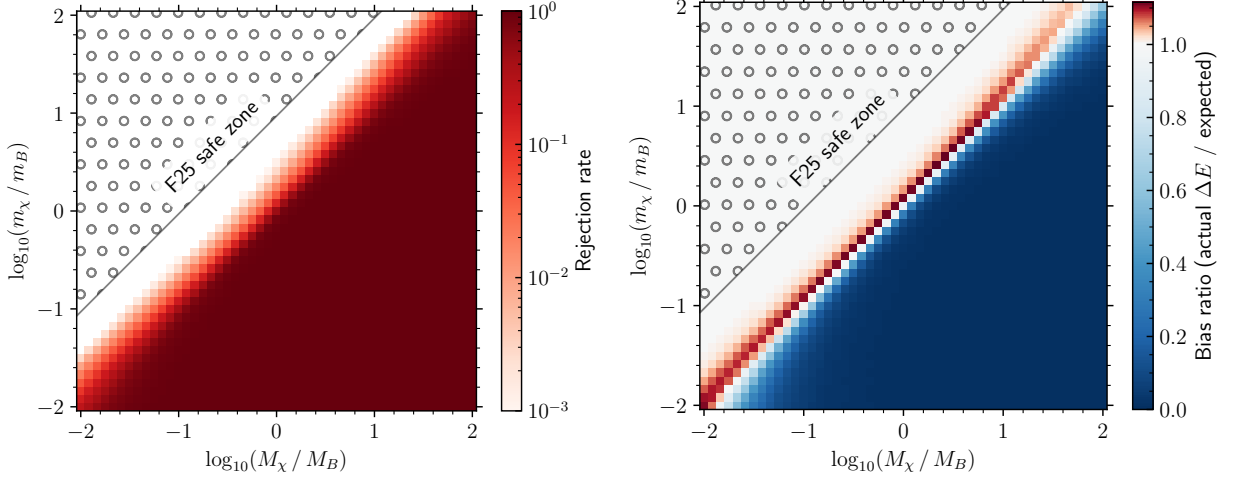


Figure 11. The expected rejection rate (left) and energy transfer bias ratio (right) of the *M. S. Fischer et al. (2025)* algorithm as a function of the mass ratios of the true particles, m_χ/m_B , and of the macroparticles, M_χ/M_B . The accuracy of the method is highly degraded whenever $M_\chi/M_B \gtrsim m_\chi/m_B$. An analytically predicted “safe zone” (Eq. 12, *M. S. Fischer et al. 2025*) is shown hatched with circles.

F. TEST DETAILS

As described in Section 3, we test our implementation with a simple but fairly generic test problem. We set up a $(10 \text{ kpc})^3$ box with periodic boundary conditions and fill it uniformly with gas and dark matter of densities ρ_B, ρ_χ . The gas cells are initialized at rest on a regular grid with internal energy set to $(3/2)(T_B^0/m_B)$, for T_B^0 an initial temperature and m_B the baryon particle mass, assumed to be constant and equal to m_p . The dark matter particles are given uniformly random positions and velocities sampled from a Maxwell-Boltzmann distribution with mean $\mathbf{V}_\chi = V_\chi^0 \hat{\mathbf{x}}$ and temperature T_χ^0 . We use N_B gas cells and N_χ dark matter particles. We then simulate the system with all physics disabled except for dark matter–baryon interactions.

We perform this test for many choices of these quantities, detailed in Table 2. The standard setup we choose is $\rho_B = \rho_\chi = 10^{10} M_\odot/\text{kpc}^3$, $T_B^0 = 10^4 \text{ K}$, $T_\chi^0 = 10^6 \text{ K}$, and $V_\chi^0 = 200 \text{ km/s}$, which is similar to the conditions near the center of our isolated disk galaxy. The simulations are then analyzed by computing the total momentum (along x), the temperature, and the energy of each component for each snapshot.

Name	m_χ	σ_0 cm ²	n	V_χ^0 km/s	T_χ^0 K	T_B^0	ρ_χ M_\odot/kpc^3	ρ_B	N_χ	N_B
Fiducial	$2 m_p$	10^{-26}	0	200	10^6	10^4	10^{10}	10^{10}	32^3	32^3
$V_\chi = 0$	$2 m_p$	10^{-26}	0	0	10^6	10^4	10^{10}	10^{10}	32^3	32^3
$T_\chi = T_B = 0$	$2 m_p$	10^{-26}	0	200	10^1	10^1	10^{10}	10^{10}	32^3	32^3
$\rho_B = 10 \rho_\chi$	$2 m_p$	10^{-26}	0	200	10^6	10^4	10^9	10^{10}	32^3	32^3
$\rho_\chi = 10 \rho_B$	$2 m_p$	10^{-26}	0	200	10^6	10^4	10^{10}	10^9	32^3	32^3
$N_\chi = 24^3$	$2 m_p$	10^{-26}	0	200	10^6	10^4	10^{10}	10^{10}	24^3	32^3
$N_\chi = N_B = 24^3$	$2 m_p$	10^{-26}	0	200	10^6	10^4	10^{10}	10^{10}	24^3	24^3
$m_\chi = 10 \text{ GeV}$	10 GeV	10^{-26}	0	200	5×10^6	10^4	10^{10}	10^{10}	32^3	32^3
$m_\chi = 100 \text{ MeV}$	100 MeV	2×10^{-27}	0	200	5×10^4	10^4	10^{10}	10^{10}	32^3	32^3
$m_\chi = 10 \text{ MeV}$	10 MeV	2×10^{-27}	0	200	5×10^3	10^4	10^{10}	10^{10}	32^3	32^3
$\sigma \sim v^{-2}$	$2 m_p$	2×10^{-33}	−2	200	10^6	10^4	10^{10}	10^{10}	32^3	32^3
$\sigma \sim v^{-4}$	$2 m_p$	5×10^{-40}	−4	200	10^6	10^4	10^{10}	10^{10}	32^3	32^3
F25 §3.4	m_p	1.6726×10^{-23}	0	0	484.6	72.69	10^7	10^7	10^5	21^3

Table 2. Parameter choices for tests; those that differ from the “fiducial” test are indicated in bold.

A simple numerical prediction for this problem can be made if the dark matter has a Maxwell-Boltzmann distribution at all times. Under this assumption, each population is described only by its bulk velocity and temperature, and the rates-of-change of these quantities are determined by a simple system of differential equations, resulting from taking the first two moments of the Boltzmann equation. (See Y. Ali-Haïmoud (2019) for details.) In this particular test problem, the fact that both species have zero bulk velocity along y and z allows us to simplify the system to the following:

$$\frac{dV_\chi}{dt} = \frac{\rho_B}{m_\chi + m_B} \mathcal{A}(V_{\chi B}; v_{\text{th}}^2) (V_B - V_\chi), \quad (\text{F62})$$

$$\frac{dV_B}{dt} = \frac{\rho_\chi}{m_\chi + m_B} \mathcal{A}(V_{\chi B}; v_{\text{th}}^2) (V_\chi - V_B), \quad (\text{F63})$$

$$\frac{dT_\chi}{dt} = \frac{\rho_B}{(m_\chi + m_B) v_{\text{th}}^2} \left[\mathcal{B}(V_{\chi B}; v_{\text{th}}^2) \frac{T_B - T_\chi}{m_\chi + m_B} + \mathcal{A}(V_{\chi B}; v_{\text{th}}^2) \frac{T_\chi}{m_\chi} V_{\chi B}^2 \right], \quad (\text{F64})$$

$$\frac{dT_B}{dt} = \frac{\rho_\chi}{(m_\chi + m_B) v_{\text{th}}^2} \left[\mathcal{B}(V_{\chi B}; v_{\text{th}}^2) \frac{T_\chi - T_B}{m_\chi + m_B} + \mathcal{A}(V_{\chi B}; v_{\text{th}}^2) \frac{T_B}{m_B} V_{\chi B}^2 \right], \quad (\text{F65})$$

where $V_{\chi B} = |V_\chi - V_B|$, $v_{\text{th}}^2 = T_B/m_B + T_\chi/m_\chi$, and \mathcal{A} and \mathcal{B} are given in Equations 16 and 17. Given choices for the densities ρ_B, ρ_χ , the dark matter mass m_χ , the cross section parameters σ_0, n , and the initial velocity distribution parameters $V_\chi^0, T_B^0, T_\chi^0$, this system of equations can be straightforwardly numerically integrated. We call the result of this integration the “naïve Maxwell-Boltzmann prediction.”

The assumption that the dark matter distribution is at all times Maxwell-Boltzmann does not (and should not) hold for the system in this test problem. However, as long as the distribution of dark matter velocities does not depart *too* far from Gaussian, we see very similar behavior between the simulation and the naïve Maxwell-Boltzmann prediction. To quantify the departure from Maxwell-Boltzmann of the dark matter velocity distribution, we use the Jarque-Bera statistic (C. M. Jarque & A. K. Bera 1980):

$$\text{JB} = \frac{1}{6} \left[S^2 + \frac{1}{4} (K - 3)^2 \right], \quad (\text{F66})$$

where S is the skewness and K is the kurtosis of the velocities. (Note that typically this is multiplied by the number of particles, which we forgo in order to compare simulations at different resolutions.) Large values of JB mean large departures from Maxwell-Boltzmann. For the analysis of our simulations, we compute JB for the dark matter velocities independently along x , y , and z for each snapshot. We then take the maximum value seen at any time along any axis as our guide for whether the Maxwell-Boltzmann assumption is satisfactory for a given test.

The simulation results and naïve Maxwell-Boltzmann predictions are summarized in Figures 12 through 14, which show the evolution of the momenta (left panel), temperatures (middle), and energies (right). Each panel shows the simulation results in blue (dark matter), pink (gas), and grey (total) solid lines, the naïve M-B prediction in a dotted green line, and the initial value of the total momentum or energy as a black dashed line. The maximum value of the Jarque-Bera statistic during the simulation is also reported for each test. Figure 12 shows the “fiducial” simulation, run with ten different random seeds in both the initial conditions generator and the seed inside GIZMO. These help to give an idea of the scatter in the results due to the stochasticity of our method. Figure 13 shows the tests that vary the experimental setup (velocities, temperature, densities, resolutions), all using the same dark matter model: mass $m_\chi = 2 m_p$, velocity-independent cross section $\sigma = 10$ mb. Figure 14 shows the remaining tests, which vary the dark matter model but all use the same experimental setup (note that we change the initial dark matter temperature to keep the velocity dispersion fixed).

In all simulations except the reduced dark matter resolution ($N_\chi = 24^3$), we see excellent conservation of the global momentum and energy, and the lack of perfect conservation in this one simulation is consistent with increased stochasticity because of the reduced resolution. All simulations show sensible behavior, with the dark matter and baryons equilibrating in both momentum and temperature. In all cases where the dark matter remains relatively Maxwell-Boltzmann (empirically, when $\max \text{JB} \lesssim 0.01$), we see excellent agreement between the simulation and the M-B prediction. For tests that attain larger JB values, the M-B prediction deviates from the simulation, usually predicting faster energy and momentum transfer than is observed in the simulation. We stress that this is a *failure of the naïve Maxwell-Boltzmann prediction* and not of the simulation: for these test setups, the dark matter really

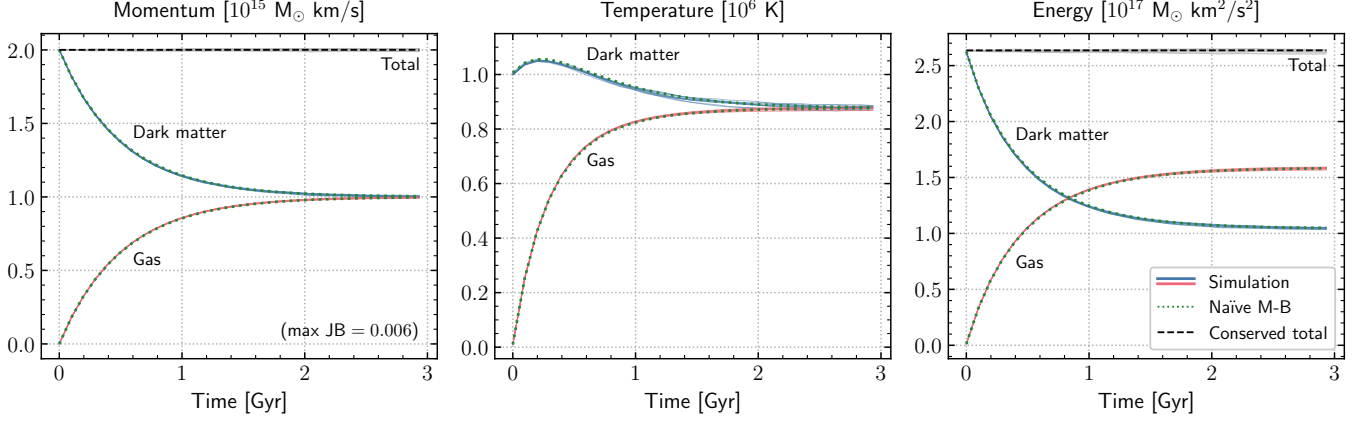


Figure 12. Global momentum along x (left), temperature (middle), and energy (right) of the components of our test simulations (solid colored) as a function of time. A black dashed line shows the initial value of the total momentum and energy in order to easily see non-conservation. A green dotted line shows a naïve analytic prediction for the evolution of the system based on an assumption that the dark matter distribution is always Maxwell-Boltzmann. The maximum value of the Jarque-Bera statistic is given (“max JB”) as an indicator of how non-thermal the dark matter distribution becomes during the test; larger values indicate larger deviations from Maxwell-Boltzmann. This figure shows the “fiducial” test, run with ten different random seeds. All tests individually show good agreement both with each other and with the M-B prediction, although some scatter is visible due to the stochastic treatment of scatterings in the dark matter. We note that the scatter is larger in the temperature and energy than the momentum, and does not appear to greatly affect the resulting gas temperatures.

does deviate from a Maxwell-Boltzmann distribution. Importantly, this suggests that assuming a Maxwell-Boltzmann distribution can be misleading for situations that arise in the evolution of galaxies. This has been similarly pointed out for the effects of dark matter–baryon interactions on linear cosmology observables (Y. Ali-Haïmoud 2019).

Serendipitously, M. S. Fischer et al. (2025) used an almost identical test setup, and included one test simulation using a constant cross section with isotropic scatterings. It was straightforward to re-create that simulation with our pipeline. The parameters used are listed in Table 2 in the final row, titled “F25 §3.4”: briefly, compared to our fiducial test, the F25 test features proton-mass dark matter, a much larger cross section, smaller densities and temperatures, lower resolution, and a longer simulation time. Figure 15 shows the results. Because the bulk velocities in this problem are zero, the global momentum plot contains no information and the temperature and energy plots are entirely redundant, so we show only the energies. We also include a zoomed-in plot of the dark matter energy and its ratio versus the naïve Maxwell-Boltzmann prediction. The behavior is indistinguishable from that reported in Figures 12 and 13 of M. S. Fischer et al. (2025), including the deviation of the simulated result from the naïve Maxwell-Boltzmann-estimated dark matter energy.

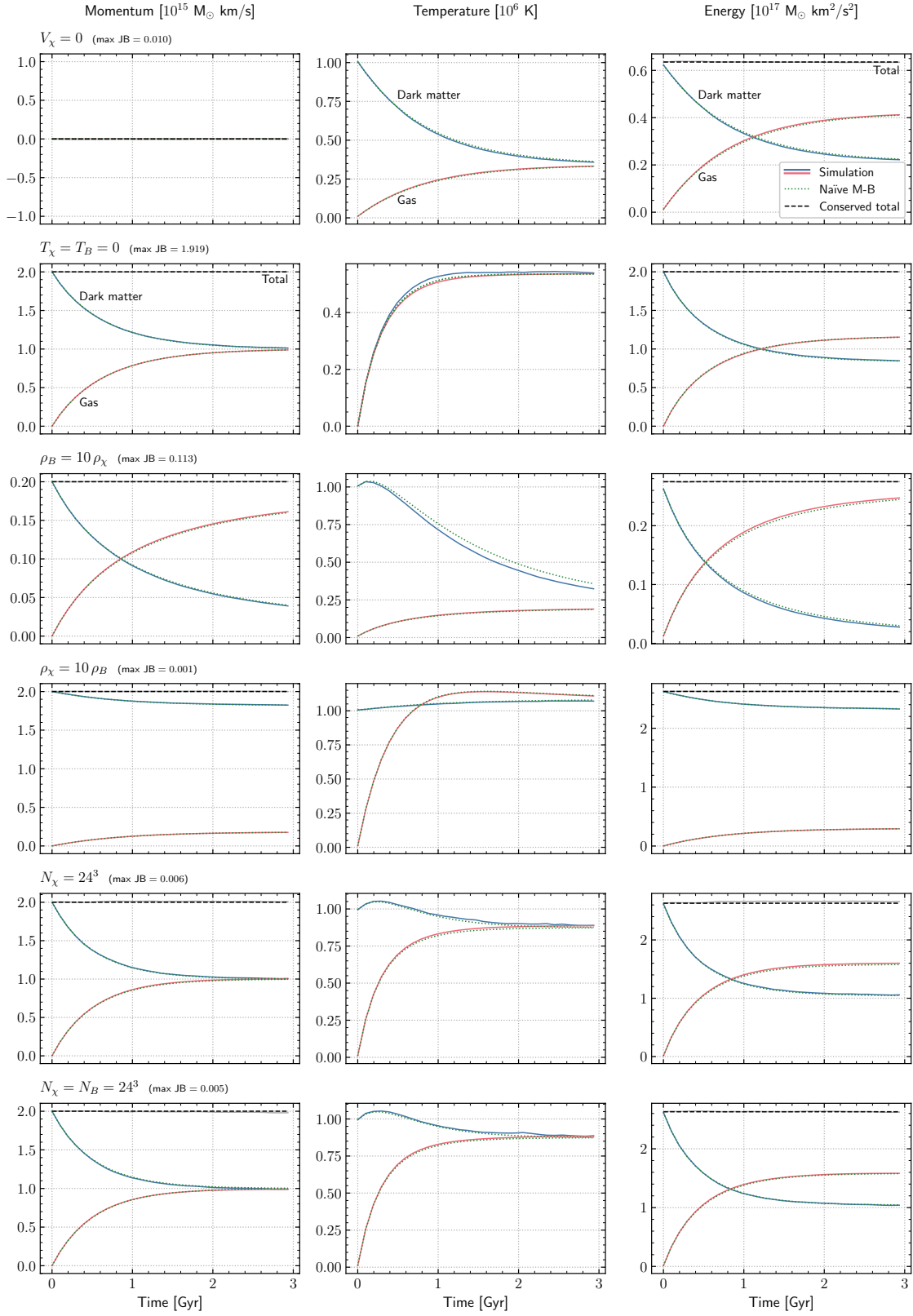


Figure 13. As in Figure 12, except varying the initial bulk velocity (top), temperatures (second row), densities (third and fourth), and resolutions (fifth and sixth).

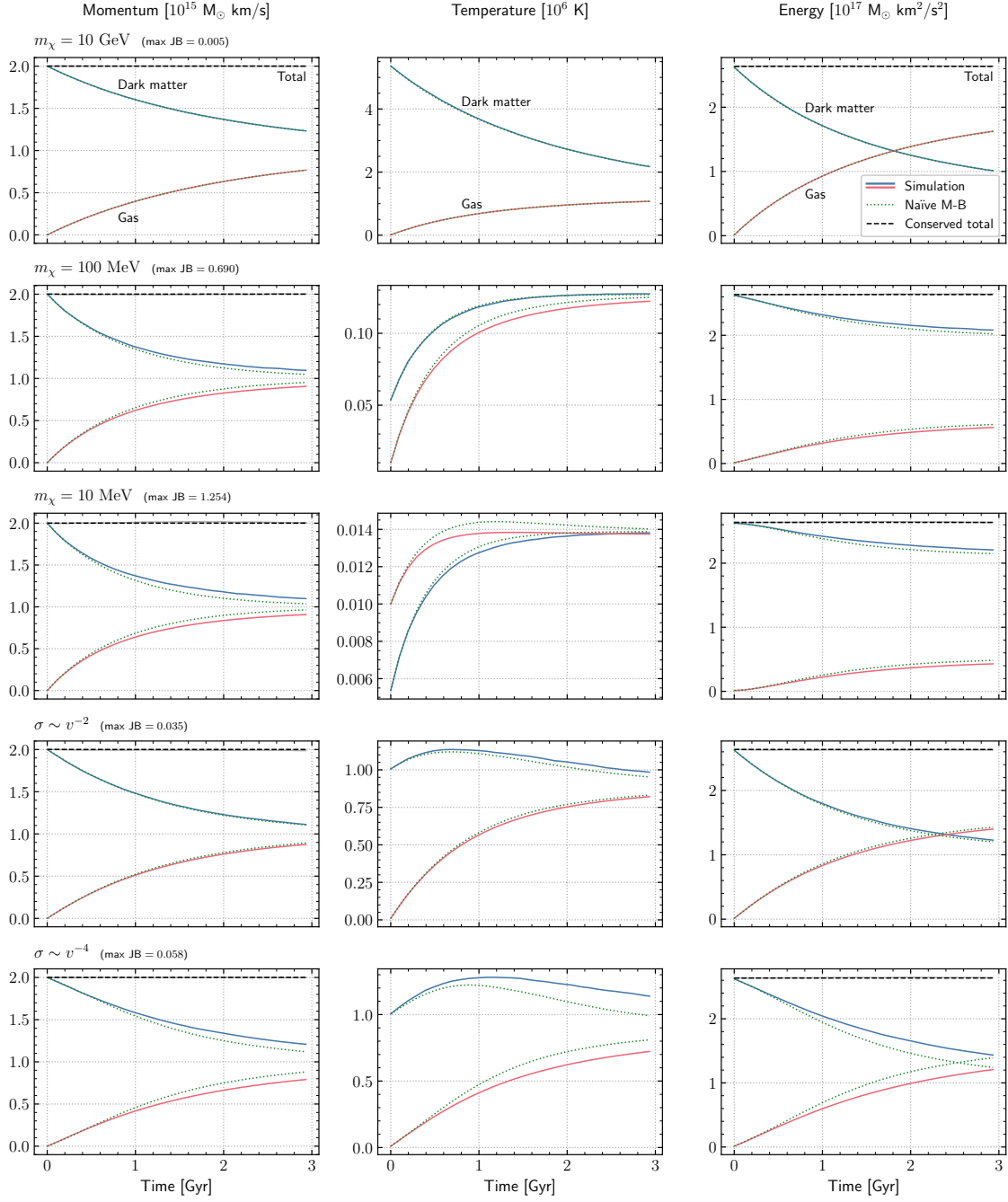


Figure 14. As in Figure 12, except varying the dark matter mass (first three rows) and velocity-dependence of the cross section (bottom two rows).

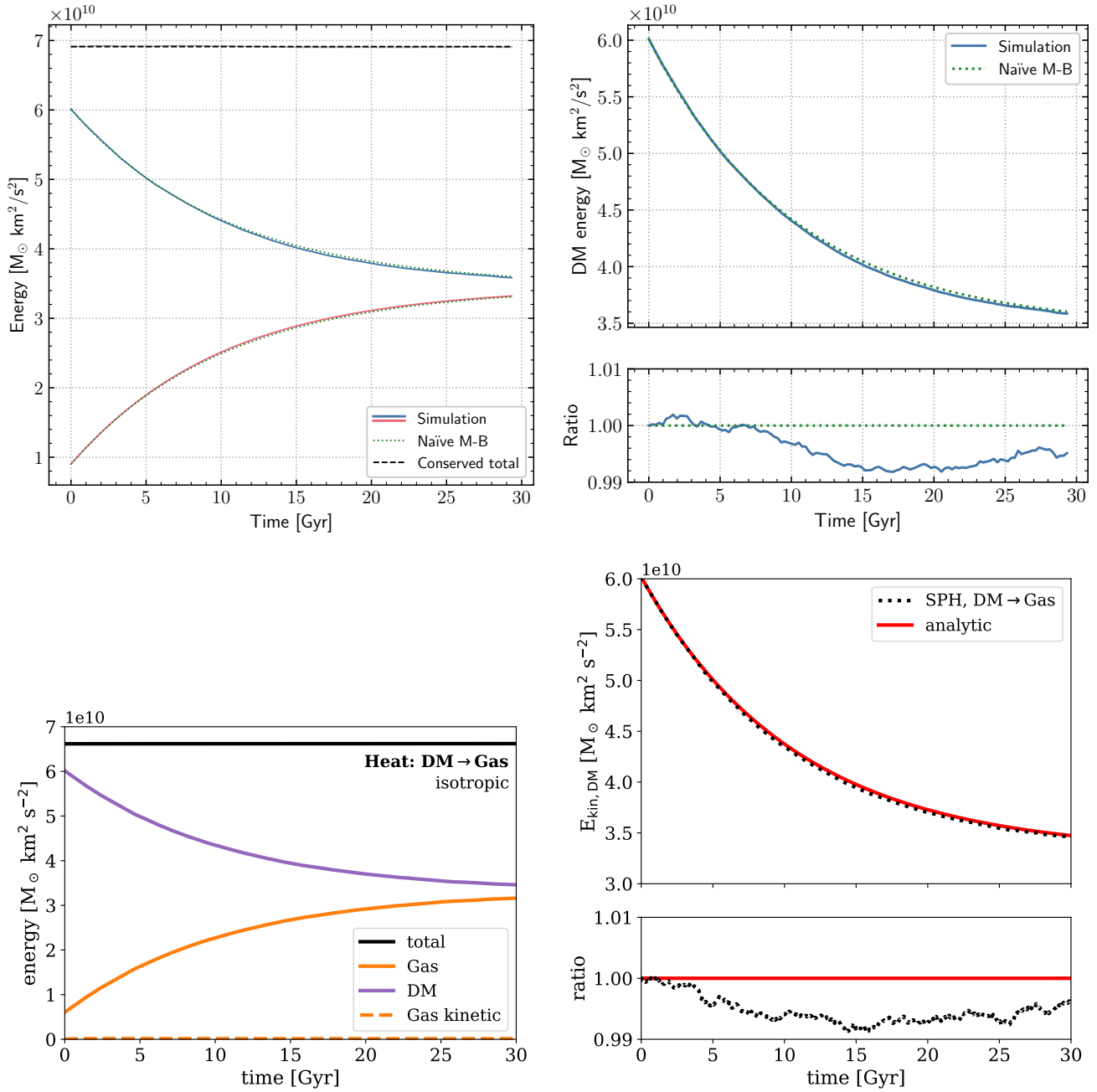


Figure 15. (Top row) Energetics of the “F25 §3.4” test problem, which re-creates the test detailed in section 3.4 of *M. S. Fischer et al. (2025)*. These plots are nearly indistinguishable from their Figures 12 and 13 (bottom row).